Structural basis for ligand recognition and G protein-coupling promiscuity of the cholecystokinin A receptor

Qiufeng Liu[1,*], Dehua Yang[1,2,3,*], Youwen Zhuang[1,*], Tristan I. Croll[4], Xiaoqing Cai[3], Antao Dai[3], Xinheng He[1,2], Jia Duan[1,2], Wanchao Yin[1], Chenyu Ye[5], Fulai Zhou[1], Beili Wu[1,2,6,7], Qiang Zhao[2,7,8], H. Eric Xu[1,2,6,†], Ming-Wei Wang[1,2,3,5,6,9,†], Yi Jiang[1,2,†]

1. The CAS Key Laboratory of Receptor Research, Shanghai Institute of Materia Medica, Chinese Academy of Sciences, Shanghai 201203, China
2. University of Chinese Academy of Sciences, Beijing 100049, China
3. The National Center for Drug Screening, Shanghai Institute of Materia Medica, Chinese Academy of Sciences, Shanghai 201203, China
4. Department of Haematology, Cambridge Institute for Medical Research, University of Cambridge, Cambridge CB2 0XY, U.K.
5. School of Pharmacy, Fudan University, Shanghai 201203, China
6. School of Life Science and Technology, ShanghaiTech University, Shanghai 201210, China
7. CAS Center for Excellence in Biomacromolecules, Chinese Academy of Sciences, Beijing 100101, China
8. State Key Laboratory of Drug Research, Shanghai Institute of Materia Medica, Chinese Academy of Sciences, Shanghai 201203, China
9. School of Basic Medical Sciences, Fudan University, Shanghai 200032, China
10. [*]These authors contributed equally: Qiufeng Liu, Dehua Yang, Youwen Zhuang

Correspondences: Y.J. (yijiang@simm.ac.cn), M.-W.W. (mwwang@simm.ac.cn), and H.E.X. (eric.xu@simm.ac.cn)

Cholecystokinin A receptor (CCK_AR) belongs to family A G protein-coupled receptors (GPCRs) and regulates nutrient homeostasis upon stimulation by cholecystokinin (CCK). It is an attractive drug target for gastrointestinal and metabolic diseases. One distinguishing feature of CCK_AR is its ability to interact with sulfated ligand and to couple with divergent G protein subtypes, including G_s, G_i, and G_q. However, the basis for G protein coupling promiscuity and ligand recognition by CCK_AR remain unknown. Here we present three cryo-electron microscopy (cryo-EM) structures of sulfated CCK-8 activated CCK_AR in complex with G_s, G_i, and G_q heterotrimers, respectively. In these three structures, CCK_AR presents a similar conformation, whereas conformational differences in "wavy hook" of Gα subunits and ICL3 of the receptor serve as determinants in G protein coupling selectivity. These structures together with mutagenesis data provide the framework for understanding the G protein coupling promiscuity by CCK_AR and uncover the mechanism of receptor recognition by sulfated CCK-8.

Cholecystokinin (CCK) is one of the earliest discovered gastrointestinal hormones, participating in gallbladder contraction and pancreatic enzyme secretion. It also acts as a neurotransmitter and is extensively distributed throughout the nervous system [1]. Selective cleavage of CCK precursor produces a series of bioactive isoforms in different lengths, with CCK-58, -33, -22, and -8 comprising the major peptide fragments in humans. However, the carboxy-terminal octapeptide CCK-8 (DYMGWMDF) is well conserved across species and is the smallest form that retains the full range of biological actions [2], mediated by two CCK receptor subtypes (CCK_AR and CCK_BR), which are present throughout the CNS and the gut. CCK_AR is primarily expressed in the alimentary tract, while CCK_BR is mainly found in the brain and the stomach [3]. CCK_AR has a ~500-fold higher affinity to CCK that has a sulfated tyrosine, whereas CCK_BR discriminates poorly between sulfated and non-sulfated CCK [4].

CCK regulates appetite and food intake primarily through CCK_AR on the vagal afferent neurons [5-8], making CCK_AR an attractive therapeutic target for obesity. However, drug development against CCK_AR is challenging, partly due to limited efficacy and safety concerns. Although several drug candidates are undergoing clinical trials, none has been approved to date [9,10]. Extensive efforts were made to elucidate the mechanism of agonism at CCK_AR through mutagenesis studies based on modeled receptor structures [11-15]. Nonetheless, the lack of precise structural information largely impedes our understanding of the molecular details regarding ligand recognition and receptor activation, thus the drug discovery targeting CCK_AR.

Most G protein-coupled receptors (GPCRs) are known to couple with a specific subtype of G proteins to elicit intracellular signal transduction [16-23]. There are four G protein subtypes, *i.e.*, stimulatory G protein (G_s), inhibitory G proteins (G_i), G_q, and $G_{12/13}$, participating in signaling pathways involving cAMP (G_s and G_i), calcium (G_q), and small G protein ($G_{12/13}$). A number of GPCR-G protein complex structures reported recently reveal that the primary determinants of G

protein coupling selectivity reside in the C-terminal α5 helix of Gα subunit and relative outward movement of TM6 [24,25]. However, CCK_AR is different from most GPCRs for its ability to couple with several subtypes of G proteins. Activation of CCK_AR elicits a diversified G protein coupling pattern [26]: predominantly G_q [27], but G_s [28], G_i [27,29], and G_{13} [30,31] all play their roles in CCK_AR signaling. This unique feature makes CCK_AR an ideal model to study G protein selectivity and promiscuity (Fig. 1a). Here, we report three cryo-EM structures of sulfated CCK-8 activated CCK_AR in complex with heterotrimeric G_q, G_s, or G_i protein, respectively. These structures reveal the unique binding mode in ligand recognition and the structural determinants responsible for G protein selectivity and promiscuity of CCK_AR.

Overall structures of CCK_AR coupled to different G proteins

The structures of sulfated CCK-8 bound CCK_AR in complex with G_q, G_s, or G_i heterotrimers were determined by single-particle cryo-EM at a global resolution of 2.9 Å, 3.1 Å, and 3.2 Å, respectively (Fig. 1, Extended Data Fig. 1, Extended Data Table 1). Sulfated CCK-8 ($DY^{SO3H}MGMWDF\text{-}NH_2$), the highest affinity natural ligand of CCK_AR [4], was used to assemble the CCK_AR-G protein complexes. Three G protein subtypes were engineered to stabilize the CCK_AR-G protein complexes (Extended Data Fig. 2). $G\alpha_q$ is chimerized by replacing its αN helix with the equivalent region of $G\alpha_{i1}$ to facilitate scFv16 binding [32]. $G\alpha_s$ was modified based on mini-$G\alpha_s$ that was used in the crystal structure determination of the G_s-coupled adenosine A_{2A} receptor ($A_{2A}R$) [33]. Two dominant-negative (DN) mutations (G203A and A326S [34]) were introduced to $G\alpha_{i1}$, and corresponding DN mutations at equivalent sites of $G\alpha_s$ and $G\alpha_q$ were also introduced (Extended Data Fig. 2b). Unless otherwise specified, G_q, G_s, and G_i refer to respective engineered G proteins, which are used in CCK_AR structure determination.

The final structures of the CCK-8–CCK_AR–G protein complexes contain sulfated CCK-8 (residues D^{1P}-F^{8P}), Gα Ras-like domain, Gβγ subunits, scFv16, and the CCK_AR residues ($E38^{N\_term}$-$F385^{8.58}$, superscripts refer to Ballesteros–Weinstein numbering [35]). The majority of amino acid side chains, including CCK-8, transmembrane domain (TMD), intracellular loops (ICLs 1-3), and extracellular loops (ECLs 1-3) were well resolved in the final models (Extended Data Fig. 3). Thus, the complex structures provide reliable details to study mechanisms of ligand recognition and G protein coupling.

Globally, CCK_AR adopts similar overall conformations in all the three structures, with the all-atom root-mean-square deviation (RMSD) at 0.84 for G_q/G_s-coupled receptors, and 1.03 for G_q/G_i-coupled receptors. The structure of the CCK-8–CCK_AR–G_q complex, which has the highest resolution at 2.9 Å, was used for detailed analysis and mechanistic evaluation of ligand recognition and receptor activation. The inactive and active structures of the closed homolog receptors (inactive: ghrelin receptor, PDB: 6KO5 [36]; active: neurotensin receptor 1, NTSR1, PDB: 6OS9 [19]), all belong to the β-branch of the rhodopsin family, are applied for structural comparison. CCK_AR presents a fully active conformation, resembling the G_i-coupled NTSR1, displaying a ~9 Å outward movement

of TM6 (measured at Cα of residue at position 6.27 in CCK_AR and ghrelin receptor) and ~4 Å inward shift of TM7 (Cα carbons of Y7.53) compared with the inactive ghrelin receptor (Extended Data Fig. 4, a and b). Similar to the active NTSR1 complex, the conserved residues in "micro-switches" (PIF, ERY, CWxP, and NPxxY) of CCK_AR display the conserved conformations observed in active GPCRs (Extended Data Fig. 4c).

Recognition of sulfated cholecystokinin

The sulfated CCK-8 occupies the orthosteric binding pocket comprised of TM3, TM4, TM5-7, and ECL1-3 (Fig. 2, Extended Data Figs. 5, 6), with its C-terminus inserting into the TMD bundle and the N-terminus facing the extracellular vestibule (Fig. 2a). The binding pocket of CCK-8 is largely overlapped with that of other reported endogenous neuropeptides, such as neurotensin (NTS_{8-13}, PDB: 6OS9 [19]), angiotensin II (Ang II, PDB: 6OS0 [37]), orexin B (OXB, PDB: 7L1U [38]), and arginine vasopressin (AVP, PDB: 7DW9 [39]). Noteworthily, the extracellular side of these neuropeptides undergo remarkable conformational shifts, while their intracellular parts converge in an approximately overlapped position at the bottom of the binding pocket (Extended Data Fig. 7).

Of interest is that the octapeptide CCK-8 almost completely occupies the polypeptide-binding pocket, structurally supporting the fact that it is the smallest active form of CCK isoforms. The binding modes of CCK-8 are highly conserved in all three CCK_AR-G protein complexes (all-atom RMSD 0.71 for CCK-8 in G_q/G_s-coupled complexes, and 1.18 for CCK-8 in G_q/G_i-coupled complexes), supported by clear EM density maps (Fig. 2a, Extended Data Fig. 3). The ligand recognition region by CCK_AR can be divided into three major parts: (i) the extracellular loops, (ii) hydrophobic cavities beneath ECLs, and (ii) the bottom of the TMD pocket (Fig. 2a).

At the extracellular side, three ECLs are folded to embrace the N-terminal amino acids of CCK-8 (Fig. 2a). The sulfate group of Y^{2P} ionic interacts with the side chain of $R197^{ECL2}$. This polar interaction prompts the aromatic ring of Y^{2P} to form hydrophobic contacts with $F185^{ECL2}$, $M195^{ECL2}$, and the main chain of $K105^{ECL1}$, thus connecting CCK-8 to ECL1 and ECL2 (Fig. 2b, Extended Data Fig. 6). These structural observations are consistent with the previous finding that the $R197^{ECL2}M$ mutation was 1,470-fold less potent than the wild-type (WT) CCK_AR [11]. The alanine mutation of $R197^{ECL2}$ completely abolishes the binding of CCK-8, thus strongly supporting the contention that $R197^{ECL2}$ serves as a determinant to discriminate between sulfated and nonsulfated CCK (Fig. 2f, Extended Data Table 2). Likewise, poor ligand selectivity of CCK_BR may be attributed to a substitution of arginine for valine at the corresponding position (Extended Data Fig. 5). Meanwhile, M^{3P}, G^{4P}, and W^{5P} clamp the interior surface of ECL3 (Fig. 2b).

Two hydrophobic cavities exist below the ECLs to accommodate M^{5P} and W^{6P} (Fig. 2c, d). The side chain of W^{5P} is sandwiched by the side chains of $I352^{7.35}$ and $R336^{6.58}$ and buries in a deep hydrophobic pocket comprised of TM6, ECL3, and TM7 (Fig. 2c). The backbone CO group of W^{5P} forms an H-bond with $R336^{6.58}$, and its indole nitrogen atom makes another H-bond with $N333^{6.55}$ (Fig. 2c, Extended Data Fig. 6), which is reported to be critical to CCK_AR activation [40]. Alanine

mutations in residues N333$^{6.55}$, R336$^{6.58}$, A343^{ECL3}, E344^{ECL3}, L347^{ECL3}, and S348^{ECL3} completely abolish the binding of CCK-8, suggesting the key roles of these residues in CCK-8 recognition (Fig. 2f, Extended Data Table 2). In contrast to the W^{5P}-occupied hydrophobic pocket, M^{6P} sits in a relatively shallow hydrophobic cavity in the opposite direction, constituted by F107^{ECL1}, C196^{ECL2}, T118$^{3.29}$, and M121$^{3.32}$ (Fig. 2d, Extended Data Fig. 6). Mutating F107^{ECL1} and residues in ECL2 and ECL3 to alanine eliminated the binding ability of CCK-8 entirely, highlighting an essential function of the three ECLs in peptide recognition (Fig. 2f, Extended Data Table 2).

At the bottom of the binding pocket, D^{7P} and main chain CO group of CCK-8 form a stabilizing polar interaction network with TM5 (H210$^{5.39}$), TM6 (N333$^{6.55}$ and R336$^{6.58}$), and TM7 (Y360$^{7.43}$) (Fig. 2e, Extended Data Fig. 6). The phenyl ring of F^{8P} makes polar hydrogen-pi interaction with Y176$^{4.60}$, and inserts into a large hydrophobic crevice comprised of residues from TM3, TM4, TM5, and TM6 (Fig. 2e, Extended Data Fig. 6). Besides N333$^{6.55}$ and R336$^{6.58}$, which also polar interact with W^{5P}, I329$^{6.51}$ is closely related to CCK-8 binding (Fig. 2f, Extended Data Table 2).

Elucidation of the recognition mechanism of CCK-8 provides clues for therapeutic development against CCK_AR. GW-5823, CE-326597, and Glaxo-11p are small molecule agonists for CCK_AR with moderate activities[10,41,42]. Docking of these agonists to the CCK_AR shows that they only occupy the bottom half of the TMD binding pocket, thus lacking essential interactions with ECLs1-3 of CCK_AR (Extended Data Fig. 8). This structural feature may lead to a weaker activity of these small molecule agonists relative to CCK-8. Together, our data provide a framework for understanding the mechanism of small molecule agonist recognition and offer a template for guiding drug design targeting CCK_AR.

Overall coupling mode of CCK_AR-G protein complexes

Although all the four G protein subtypes were reported to interact with CCK_AR [26], only three of the CCK_AR–G protein samples (CCK_AR–G_q, CCK_AR–G_s, and CCK_AR–G_i protein complexes) were obtained for high-resolution cryo-EM structure determination (Fig. 1). Structural comparison indicated that TM6 and ICL2 in CCK_AR adopt nearly identical conformations in G_q-, G_i-, and G_s-coupled structures (Fig. 3a, Extended Data Fig. 7). However, slightly different tilts of the Gα α5 helix were seen among the three heterotrimeric G proteins (4° for $G\alpha_q$/$G\alpha_s$ and 8° for $G\alpha_q$/$G\alpha_i$) (Fig. 3a). Meanwhile, the distal end of $G\alpha_s$ α5 helix moves 7 Å outward away from the TMD core relative to the equivalent $G\alpha_q$ residue (measured at Cα atom of L$^{H5.25}$, superscript refers to CGN system [43]) (Fig. 3a). The G_q presents the largest solvent-accessible surface area (SASA, 1492 Å^2) with the receptor compared to G_s (1293 Å^2) and G_i (1167 Å^2), consistent with a 6.6- to 20.3-fold increased potency of G_q coupling to CCK_AR in comparison to that coupled with G_s and G_i (Extended Data Fig. Table 3). This finding supports the hypothesis that the size of the G protein coupling interface may correlate with the ability of a receptor to link with different G proteins [23,24]. In addition, coupling of different G protein subtypes exhibits distinct effects on CCK-8 binding. Compared to G_s or G_i proteins, G_q coupling increases the binding affinity of CCK-8 (Extended Data Table 3), consistent

with the increased binding activity of isoproterenol against $\beta_{2A}R$ in the presence of G_s protein [16]. This finding indicates an allosteric modulation effect of G_q protein on CCK-8 binding, supporting the positive cooperativity between agonists and G proteins [44].

In addition, comparisons of these three complex structures to previously reported G protein-coupled class A GPCRs reveal the different extent of TM6 displacement and concomitant shift of Gα α5 helix (Fig. 3b-d). TM6 of CCK_AR in all three G protein complexes displays an 11-12 Å (measured at Cα atom of residue at position 6.27) smaller outward displacement in contrast to G_s-coupled GPCRs, which translates into a notable swing of Gα α5 helix in the same direction (9-11° relative to G_s-coupled $\beta_{2A}R$ and $A_{2A}R$ as measured at Cα atom of $Y^{H5.23}$). This smaller displacement of TM6 is contrary to the previous assumption that TM6 of G_s-coupled GPCRs undergoes a significant outward movement, thus opening a larger cytoplasmic pocket to accommodate bulkier residues at the distal end of $G\alpha_s$ α5 helix relative to $G_{i/o}$-coupled receptors [23,45]. To avoid a potential clash with TM6, the distal end of the $G\alpha_s$ α5 helix in the CCK_AR–G_s complex stretches away from the TMD core and inserts into the crevice between TM6 and TM7–helix 8 joint. This featured conformation of $G\alpha_s$ α5 helix in the CCK_AR–G_s complex is unique compared to that in structures of the G_s-coupled $\beta_{2A}R$ and $A_{2A}R$, supporting the complexity of GPCR-G protein coupling mechanism (Fig. 3b).

TM6 and Gα α5 helix of CCK_AR–G protein complexes display similar conformational changes to other G_i- and G_q-coupled GPCRs, such as the G_i-coupled NTSR1 and the G_q-coupled 5-$HT_{2A}R$ (Fig. 3c, d). TM6 of CCK_AR–G_i protein complex is highly overlaid with that of G_i-coupled NTSR1, while the cytoplasmic end of TM6 shows a 4 Å smaller outward displacement compared to that of G_o-coupled M_2R (Fig. 3c). On the G protein side, the α5 helix of $G\alpha_i$ in the CCK_AR–G_i complex shows a nearly overlapped conformation compared to that of the NTSR1–G_i complex. In contrast, it exhibits a 3 Å (measured at Cα atom of $Y^{H5.23}$) shift away from TM6 relative to that of G_o-coupled M_2R (Fig. 3c). Structural comparison of G_q-coupled CCK_AR with G_q/G_{11}-coupled GPCRs demonstrates a 2 Å (measured at Cα atom of $Y^{H5.23}$) upward toward the cytoplasmic cavity in contrast to the G_q-coupled 5-$HT_{2A}R$ and a 28° rotation away from TM6 relative to G_{11}-coupled M_1R (Fig. 3d).

Interaction patterns for the "wavy hook" of the CCK_AR-G protein complexes

The "wavy hook" at the extreme C-terminus of the Gα α5 helix is thought to be one of the coupling specificity determinants for G protein [46,47], which undergoes distinct conformational rearrangements among the three CCK_AR–G protein complexes (Fig. 3a).

A structural comparison of the interaction interface between the receptor cytoplasmic cavity and Gα "wavy hook" reveals distinct features of CCK_AR–G protein coupling. Well-defined densities of Gα protein "wavy hook" residues allow for detailed structural analyses except for residues at the -1 position. $L(-2)^{H5.25}$ in α5 helix is highly conserved across the G protein families and plays a pivotal role in G protein coupling. Both $L358^{H5.25}$ in $G\alpha_q$ and $L353^{H5.25}$ in $G\alpha_i$ hydrophobically

interact with residues in TM3 and TM6 (R139$^{3.50}$, I143$^{3.54}$, V311$^{6.33}$, and L315$^{6.37}$) (Fig. 4a, b). Due to the notable displacement of $G\alpha_s$ C-terminus, L393$^{H5.25}$ in $G\alpha_s$ moves 7 Å outward away from the TMD core relative to the equivalent $G\alpha_q$ residue (Fig. 3a), repositioning it in a hydrophobic sub-pocket formed by M314$^{6.36}$ and M373$^{7.56}$ (Fig. 4c). In contrast to L(-2)$^{H5.25}$, residues at positions H(-3)$^{5.24}$, H(-4)$^{5.23}$ and H(-5) $^{5.22}$ are less conserved. N357(-3)$^{H5.24}$ in $G\alpha_q$ makes an H-bond with the backbone CO group of Y370$^{7.53}$ (Fig. 4a). Owing to the replacement of $G\alpha_i$ G352(-3)$^{H5.24}$ and the reposition of $G\alpha_s$ E392(-3)$^{H5.24}$, the corresponding H-bond is absent in CCK_AR–G_i and CCK_AR–G_s complex structures. Additionally, Y356(-4)$^{H5.23}$ in $G\alpha_q$ forms extensive interactions with the receptor cytoplasmic cavity by making H-bonds with R139$^{3.50}$ and Q153^{ICL2} (Fig. 4d). In contrast, C351(-4)$^{H5.23}$ in $G\alpha_i$ only forms a weak H-bond with R139$^{3.50}$ via its backbone CO group (Fig. 4e). Y391(-4)$^{H5.23}$ in $G\alpha_s$ exhibits limited hydrophobic and Van der Waals interactions with residues in TM2 and TM3 (T76$^{2.39}$, R139$^{3.50}$, and A142$^{3.53}$) (Fig. 4f). Furthermore, both E355(-5)$^{H5.22}$ in $G\alpha_q$ and D350(-5)$^{H5.22}$ in $G\alpha_i$ form salt bridges with R376$^{8.49}$ in CCK_AR, while Q390(-5) $^{H5.22}$ in $G\alpha_s$ disfavors the formation of corresponding electrostatic interaction (Fig. 4d-f). To understand the "wavy hook" mediated G-protein selectivity, we displaced the amino acids (H5.22-H5.25) in $G\alpha_q$ subunit with the corresponding ones in $G\alpha_s$ and $G\alpha_i$ subunits. BRET assay results show that the $G\alpha_i$ displacement has no impact on CCK_AR-G protein coupling compared to wild-type $G\alpha_q$ subunit. However, partially (E355Q or N357E) or completely $G\alpha_s$ substitution remarkably decreased the G protein coupling activity of CCK_AR (Fig. 4g). These results indicate that the "wavy hook" may play a crucial role in coupling selectivity of CCK_AR with G_q over G_s protein.

Contribution of CCK_AR ICL3 to G_q-coupling selectivity

In the CCK_AR–G_q protein complex structure, CCK_AR displays a comparable length of TM5 relative to M_1R–G_{11} complex [21]. However, the cytoplasmic end of CCK_AR TM5 exhibits an 8 Å outward bend (measured at Cα atoms of A$^{5.73}$), which prevents it from interacting with the $G\alpha_q$ subunit (Fig. 5a). Instead, the ICL3 inserts into the cleft between TM5 of CCK_AR and α5 helix of the $G\alpha_q$ subunit (Fig. 5a). Compared to L225$^{5.75}$ in M_1R, I296^{ICL3} in CCK_AR interacts with the same hydrophobic patch formed by side chains of Y325$^{S6.02}$, F339$^{H5.06}$, and A342$^{H5.09}$ in $G\alpha_q$ subunit, but is buried deeper to create more closely packed hydrophobic contacts (Fig. 5a, b). These hydrophobic interactions are critical to CCK_AR–G_q coupling, as evidenced by our BRET analysis that I296^{ICL3}G mutation significantly weakened G_q coupling to CCK_AR but had no impact on G_s and G_i coupling (Fig. 5c, Extended Data Table 4). This hydrophobic patch that lies on the outer surface may be unique for the $G_{q/11}$ subunit. The equivalent residues in $G\alpha_s$ and $G\alpha_i$ subunits are polar or charged residues, which would be energetically unfavorable to form hydrophobic interactions (Extended Data Fig. 10). Indeed, this unconventional ICL3-G_q interaction is not seen in the structures of G_s- and $G_{i/o}$-coupled CCK_ARs (Fig. 3b, c). Together, our findings offer structural evidence on the possible role of ICL3 in CCK_AR–G_q coupling preference. Hydrophobic residues on the inner surface of the ICL3 loop of CCK_AR or the extended TM5 of M_1R may represent a common feature of $G_{q/11}$-

coupled GPCRs.

Conclusions

As the largest family of cell surface receptors, GPCRs have more than 800 members but only couple to four G protein subtypes. Specific GPCR signaling requires the receptor to couple with either a single or multiple G protein subtypes [47-49]. Thus, one of the main questions is how does a given GPCR select a G protein subtype for downstream signal transduction. The critical G protein determinants of selectivity vary widely for different receptors that couple to specific G proteins. It is thought that G_s- or G_q-coupled receptors are relatively promiscuous and to some extent couple to G_{i1} [24]. However, G_i-coupled receptors are more selective [24]. The minor outward movement of TM6 contributes to such a superior G_i-coupling selection as opposed to that of G_s [18,25,46,50,51]. Although proven to be promiscuous, G_q-coupled receptors tend to adopt an active conformation similar to that of G_i-coupled GPCRs, reflecting the complexity of the GPCR-G protein coupling mechanism [21,22]. Since CCK_AR has the ability to couple with different G protein subtypes, it stands out as a suitable model for studying the promiscuity of G protein coupling. In this paper, we show that TM6 of CCK_AR undergoes a similar outward displacement relative to $G_{i/o}$-coupled (NTSR1 and M_2R) and $G_{q/11}$-coupled GPCRs (5-$HT_{2A}R$ and M_1R) but has a smaller shift relative to G_s-coupled GPCRs ($\beta_{2A}R$ and $A_{2A}R$). CCK_ARs share almost identical conformations, whereas G_q, G_s, and G_i proteins vary in distinct orientations, producing different sizes of receptor-G protein interface. The predominant coupling to G_q by CCK_AR can be explained by the largest interface among three CCK_AR-G protein complexes. Structural comparison of the three CCK_AR–G protein complexes reveals that “wavy hook” residues of Gα α5 helix and ICL3 of the receptor are important for the coupling promiscuity. In addition, detailed inspections disclose structural clues relative to the recognition mechanism of sulfated CCK-8 by CCK_AR, in which $R197^{ECL2}$ is a major determinant. Together, our structures provide a framework for better understanding of ligand recognition as well as G protein coupling selectivity and promiscuity by CCK_AR.

Methods

Expression and purification of CCK_AR-G protein complexes

The WT CCK_AR (residues 1-428) was applied for cryo-EM studies. The full-length CCK_AR cDNA was cloned into a modified pFastBac vector (Invitrogen) containing a hemagglutinin (HA) signal sequence followed by an 8× histidine tag, a double-MBP tag, and a TEV protease site before the receptor sequence using homologous recombination (CloneExpress One Step Cloning Kit, Vazyme) (Extended Data Fig. 2a). The N-terminal 1-29 amino acids of $G\alpha_q$ was replaced by the equivalent residues of $G\alpha_{i1}$ to facilitate the scFv16 binding [21]. An engineered $G\alpha_s$ construct was generated based on mini-$G\alpha_s$ [33]. The N-terminal 1-18 amino acids and α-helical domain of $G\alpha_s$ were replaced by human $G\alpha_{i1}$, thus providing binding sites for scFv16 and Fab-G50, respectively [18,21]. Additionally, human $G\alpha_{i1}$ with two dominant-negative mutations (G203A and A326S [34]) was used to assemble a

stable GPCR-G_i protein complex. These two cognate mutations also exist in engineered $G\alpha_q$ and $G\alpha_s$ (Extended Data Fig. 2b). Receptor, rat H6-Gβ, bovine Gγ, and the specific Gα subunit were co-expressed in *Spodoptera frugiperda* (*sf*9) insect cells (Invitrogen) as previously described [52]. In addition, GST-Ric-8A (a gift from Dr. B. Kobilka) was applied to improve the expression of $G\alpha_q$.

ScFv16 was applied to improve the protein stability of CCK_AR–G_q and CCK_AR–G_i complex samples. The monomeric scFv16 was prepared as previously reported [53]. Cell pellets of the co-expression culture were thawed and lysed in 20 mM HEPES, pH 7.4, 100 mM NaCl, 10% glycerol, 5 mM $MgCl_2$, and 10 mM $CaCl_2$ supplemented with EDTA-free protease inhibitor cocktail (TargetMol). CCK_AR–G protein complexes were assembled at room temperature (RT) for 1 h by the addition of 10 μM CCK-8 (GenScript) and 25 mU/mL apyrase. Then the lysate was solubilized in 0.5% LMNG, 0.1% CHS, and the soluble fraction was purified by nickel affinity chromatography (Ni Smart Beads 6FF, SMART Lifesciences). In the case of CCK_AR–G_i and CCK_AR–G_q complexes, a 3 molar excess of scFv16 was added to the protein elute. The mixture was incubated with amylose resin for 2 h at 4°C. The excess G protein and scFv16 were washed with 20 column volumes of 20 mM HEPES, pH 7.4, 100 mM NaCl, 10% glycerol, 0.01% LMNG, 0.002% CHS, and 2 μM CCK-8. TEV protease was then included to remove the N terminal fusion tags of CCK_AR. After 1 h incubation at RT, the flow-through was collected, concentrated, and injected onto a Superdex 200 10/300 column equilibrated in the buffer containing 20 mM HEPES, pH 7.4, 100 mM NaCl, 0.00075% LMNG, 0.00025% GDN, 0.0002% CHS, and 10 μM CCK-8. The monomeric complex peak was collected and concentrated to about 5 mg/mL for cryo-EM studies.

Cryo-EM grid preparation and image collection

For preparation of cryo-EM grids, 2.5 μL of each purified CCK_AR–G protein complex was applied individually onto the glow-discharged holey carbon grids (Quantifoil, Au300 R1.2/1.3) in a Vitrobot chamber (FEI Vitrobot Mark IV). The Vitrobot chamber was set to 100% humidity at 4°C. Extra samples were blotted for 2 s and were vitrified by plunging into liquid ethane. Grids were stored in liquid nitrogen for condition screening and data collection usage.

Automatic data collection of CCK-8–CCK_AR–G protein complexes were performed on a FEI Titan Krios operated at 300 kV. The microscope was operated with a nominal magnification of 81,000× in counting mode, corresponding to a pixel size of 1.045 Å for the micrographs. A total of 5,415 movies for the dataset of CCK-8–CCK_AR–G_q–scFv16 complex, 5008 movies for the dataset of CCK-8–CCK_AR–G_s complex, and 4,811 movies for the dataset of CCK-8–CCK_AR–G_i–scFv16 complex were collected, respectively, by a Gatan K3 Summit direct electron detector with a Gatan energy filter (operated with a slit width of 20 eV) (GIF) using the SerialEM software. The images were recorded at a dose rate of about 26.7 e/Å^2/s with a defocus ranging from -0.5 to -3.0 μm. The total exposure time was 3 s and intermediate frames were recorded in 0.083 s intervals, resulting in a total of 36 frames per micrograph.

Image processing and map reconstruction

Image stacks were subjected to beam-induced motion correction and aligned using MotionCor 2.1. Contrast transfer function (CTF) parameters were estimated by Ctffind4. The data processing was performed using RELION-3.0 [54]. The micrographs with the measured resolution worse than 4.0 Å and micrographs imaged within carbon area were discarded, generating 3,806 micrographs for CCK-8–CCK_AR–G_q–scFv16 dataset, 4,963 micrographs for CCK-8–CCK_AR–G_s dataset, and 4,543 micrographs for CCK-8–CCK_AR–G_i–scFv16 dataset for further data processing. Particle selection, 2D and 3D classifications were performed on a binned dataset with a pixel size of 2.09 Å. About 2,000 particles were manually selected and subjected to 2D classification. Representative averages were chosen as template for particle auto-picking. The auto-picking process produced 3,405,355 particles for CCK-8–CCK_AR–G_q–scFv16 complex, 4,680,972 particles for CCK-8–CCK_AR–G_s complex, and 4,270,010 particles for CCK-8–CCK_AR–G_i–scFv16 complex, which were subjected to reference-free 2D classifications to discard bad particles. Initial reference map models for 3D classification were generated by Relion using the representative 2D averages. For CCK-8–CCK_AR–G_q–scFv16 complex, the particles selected from 2D classification were subjected to 6 rounds 3D classifications, resulting in a single well-defined subset with 555,628 particles. For CCK-8–CCK_AR–G_s complex, the particles resulting from 2D classification were subjected to 5 rounds 3D classifications, resulting in two well-defined subsets with 499,924 particles. For CCK-8–CCK_AR–G_i–scFv16 complex, the particles selected from 2D classification were subjected to 7 rounds 3D classifications, resulting in two well-defined subsets with 140,602 particles. Further 3D refinement, CTF refinement, Bayesian polishing and DeepEnhancer processing generated density maps with an indicated global resolution of 2.9 Å for CCK-8–CCK_AR–G_q–scFv16 complex, 3.1 Å for CCK-8–CCK_AR–G_s complex, and 3.2 Å for CCK-8–CCK_AR–G_i–scFv16 complex, respectively, at a Fourier shell correlation of 0.143.

Model building and refinement

For the CCK_AR–G_q complex, the initial G_q protein and scFv16 model were adopted from the cryo-EM structure of the M_1R–G_{11} protein complex (PDB: 6OIJ) [21]. The initial CCK_AR model was generated by an online homology model building tool [55]. All models were docked into the EM density map using Chimera [56], followed by iterative manual adjustment and rebuilding in COOT [57] and ISOLDE [58], and real-space refinement using Phenix programs [59]. The model statistics were validated using Phenix comprehensive validation. A model of the refined CCK_AR from the CCK_AR–G_q complex was used for the other two complexes. Models from PTH1R–G_s (PDB: 6NBF) and FPR2–G_i (PDB: 6OMM) were used as templates for the model building of G_s in the CCK_AR–G_s complex and G_{i1}–scFv16 in the CCK_AR–G_i complex, respectively. Then the fitted models were built the same way as the CCK_AR–G_q complex. The final refinement statistics are provided in Extended Data Table 1.

Radiolabeled ligand-binding assay

The WT or mutant CCK_ARs were transiently transfected into HEK 293T/17 cells (purchased from the Cell Bank at the Chinese Academy of Sciences) which were cultured in poly-D-lysine coated 96-well plate. Twenty-four h later, the cells were washed twice and incubated with blocking buffer (DMEM medium supplemented with 33 mM HEPES, and 0.1% (w/v) BSA, pH 7.4) for 2 h at 37°C. After three times washes by cold-ice PBS, the cells were treated by a constant concentration of ^{125}I-CCK-8 (40 pM, PerkinElmer) plus 8 different doses of CCK-8 (1 pM to 10 μM) for 3 h at RT. Cells were washed three times with ice-cold PBS and lysed by 50 μL lysis buffer (PBS supplemented with 20 mM Tris-HCl and 1% (v/v) Triton X-100, pH 7.4). Subsequently, the plates were counted for radioactivity (counts per minute, CPM) in a scintillation counter (MicroBeta^2 plate counter, PerkinElmer) using 150 μl scintillation cocktail (OptiPhase SuperMix, PerkinElmer).

G protein dissociation assay

G protein dissociation was monitored by BRET (bioluminescence resonance energy transfer) experiments performed as previously reported [60]. Briefly, a C-terminal fragment of the GRK3 (GRK3ct) fused to a luciferase serves as a BRET donor. Gβγ dimer is labeled with a fluorescent protein Venus, a BRET acceptor. Upon G protein heterotrimer activation, free Gβγ-Venus is released and binds to membrane-associated GRK3ct-luciferase, leading to an increased signal detectable by BRET.

HEK 293T/17 cells were seeded onto 10 μg/mL Matrigel-coated 6-well plate (1×10^6 cells/well). After 4 h culture, WT or mutant CCK_AR (0.84 μg), Gα ($G\alpha_q$, $G\alpha_s$, and $G\alpha_i$, 2.1 μg each), Gβ (0.42 μg), Gγ (0.42 μg), and GRK (0.42 μg) were transiently transfected with Lipofectamine™ LTX Reagent (Invitrogen). Twenty-four hours post-transfection, cells were washed once with DMEM medium (no phenol red) and detached by EDTA. Cells were then harvested with centrifugation at 1000 rpm for 5 min and resuspended in DMEM medium. Approximately 75,000 cells per well were distributed in 96-well flat-bottomed white microplates (PerkinElmer). The NanoBRET substrate (furimazine, 25 μL/well, Promega) was added, and the BRET signal (535 nm/475 nm ratio) was determined using an EnVision multilabel plate reader (PerkinElmer). The average baseline value recorded before CCK-8 stimulation was subtracted from BRET signal values.

NanoBiT G-protein recruitment assay

The recruitment of CCK_AR to G_i-protein was detected in *sf9* cells using NanoBiT method as previously reported [61]. Briefly, the LgBiT fragment of NanoBiT luciferase was fused to the C-terminus of CCK_AR. SmBiT was fused to the C-terminus of Gβ subunit with a 15-amino acid flexible linker. CCK_AR-LgBiT, $G\alpha_{i1}$, SmBiT-fused human Gβ1 and human Gγ2 were co-expressed in *sf9* insect cells. Cell pellets were collected by centrifugation after infection for 48 h. The cell suspension was dispensed in a 96-well plate (64,000 cells per well) at a volume of 80 μL diluted in the assay buffer (HBSS buffer supplemented with 10 mM HEPES, pH 7.4) and incubated for 30

min at 37°C. The cells were then reacted with 10 μL of 50 mM coelenterazine H (Yeasen) for 2h at RT. Luminescence signal was measured using an EnVision plate reader (PerkinElmer) at 30 s intervals (25°C). The baseline was measured before CCK-8 addition for 8 intervals, and the measurements continued for 20 intervals following ligand addition. Data were corrected to baseline measurements and the results were analyzed using GraphPad Prism 8.0 (Graphpad Software Inc.).

NanoBiT G-protein dissociation assay

G_s activation was measured by a NanoBiT dissociation assay. G protein NanoBiT split luciferase constructs were generated by fusing the LgBiT in $G\alpha_s$ and the SmBiT to Gγ (a gift from Dr. Asuka Inoue, Tohoku University) as previously reported [62]. In brief, HEK 293T/17 cells were plated in 10 cm plates at a density of 3×10^6 cells per plate. After 24 h, cells were transfected with 1.62 μg plasmids of receptor, 0.81 μg $G\alpha_s$-LgBiT, 4.1 μg Gβ, and 4.1 μg SmBiT-Gγ using Lipofectamine™ LTX Reagent (Invitrogen). The transiently transfected cells were then seeded into poly-D-lysine coated 96-well plates (50,000 cells per well) and grown overnight before incubation in an assay buffer. The measurement of luminescence signal was identical to the steps described above.

Surface expression assay

HEK 293T/17 cells were seeded into a 6-well plate and incubated overnight. After transient transfection with WT or mutant plasmids for 24 h, the cells were collected and blocked with 5% BSA in PBS at RT for 15 min and incubated with primary anti-Flag antibody (1:300, Sigma-Aldrich) at RT for 1 h. The cells were then washed three times with PBS containing 1% BSA followed by 1 h incubation with donkey anti-mouse Alexa Fluor 488-conjugated secondary antibody (1:1000, ThermoFisher) at 4°C in the dark. After three washes, the cells were resuspended in 200 μl of PBS containing 1% BSA for detection in a NovoCyte flow cytometer (ACEA Biosciences) utilizing laser excitation and emission wavelengths of 488 nm and 519 nm, respectively. For each assay point, approximately 15,000 cellular events were collected, and the total fluorescence intensity of positive expression cell population was calculated.

Molecular docking

Before docking, hydrogens were added to CCK_AR and the whole system coordinates were optimized with a pH of 7.0. A grid file was then generated on the peptide pocket in our G_q-coupled CCK_AR structure. Small molecule ligands Glaxo-11p, GW-5823, and CE-326597 were prepared in the OPLS3 force field with a pH of 7.0 to generate 3D structures. Finally, glide docking with standard precision was applied to all ligands and the structures with the best docking score were picked as outputs.

Acknowledgments

We thank Kirill A. Martemyanov for expert advice on BRET assay. The cryo-EM data were

collected at the Cryo-Electron Microscopy Research Center, Shanghai Institute of Materia Medica (SIMM). The authors thank the staff at the SIMM Cryo-Electron Microscopy Research Center for their technical support. **Funding:** This work was partially supported by the Ministry of Science and Technology (China) grant 2018YFA0507002 (H.E.X.) and 2018YFA0507000 (M.-W.W.); National Natural Science Foundation of China 31770796 (Y.J.), 81872915 (M.-W.W.), 81773792 (D.Y.), and 81973373 (D.Y.); National Science and Technology Major Project of China – Key New Drug Creation and Manufacturing Program 2018ZX09735–001 (M.-W.W.), 2018ZX09711002-002-002 (Y.J.), and 2018ZX09711002–002–005 (D.Y.); Shanghai Municipal Science and Technology Commission Major Project 2019SHZDZX02 (H.E.X.); the Strategic Priority Research Program of Chinese Academy of Sciences (XDB37030103 to H.E.X.); Shanghai Sailing Program 19YF1457600 (Q.F.L.); Wellcome Trust Principal Research Fellowship 209407/Z/17/Z (T.C.); and Novo Nordisk-CAS Research Fund grant NNCAS-2017–1-CC (D.Y.).

Author contributions

Q.F.L. screened the expression constructs, optimized the CCK_AR-G protein complexes, prepared the protein samples for final structure determination, participated in cryo-EM grid inspection and data collection, built and refined the structure models, prepared the constructs for functional assays, analyzed the structures, and prepared the figures and wrote the initial manuscript; Y.W.Z. performed cryo-EM grid preparation, data collection, structure determination, and participated in protein sample optimization, figure and manuscript preparation; T.C. helped build and refine the structure model; X.H.H. performed the molecular docking; J.D. and W.C.Y. designed G protein constructs; F.L.Z. participated in data analysis; B.L.W. and Q.Z. participated in research supervising; H.E.X. conceived and supervised the project, analyzed the structures, and initiated collaborations with M.-W.W., supervised Q.F.L., Z.Y.W., F.L.Z., J.D., W.C.Y.; M.-W.W and D.H.Y. supervised X.Q.C., A.T.D., and C.Y.Y. in G protein assay development and data analysis; M.-W.W. participated in manuscript writing; Y.J. supervised the studies, performed the structural analysis, and prepared the figures and wrote the manuscript with input from all co-authors.

Competing interests

All authors declare no competing interests.

Data availability

All data is available in the main text or the supplementary materials. Materials are available from the corresponding authors upon reasonable request.

References

1 Bowers, M. E., Choi, D. C. & Ressler, K. J. Neuropeptide regulation of fear and anxiety: Implications of cholecystokinin, endogenous opioids, and neuropeptide Y. Physiol Behav 107,

699-710, doi:10.1016/j.physbeh.2012.03.004 (2012).

2 Rehfeld, J. F., Friis-Hansen, L., Goetze, J. P. & Hansen, T. V. The biology of cholecystokinin and gastrin peptides. Curr Top Med Chem 7, 1154-1165, doi:10.2174/156802607780960483 (2007).

3 Wank, S. A. Cholecystokinin receptors. Am J Physiol 269, G628-646, doi:10.1152/ajpgi.1995.269.5.G628 (1995).

4 Dufresne, M., Seva, C. & Fourmy, D. Cholecystokinin and gastrin receptors. Physiol Rev 86, 805-847, doi:10.1152/physrev.00014.2005 (2006).

5 Moran, T. H., Smith, G. P., Hostetler, A. M. & McHugh, P. R. Transport of cholecystokinin (CCK) binding sites in subdiaphragmatic vagal branches. Brain Res 415, 149-152, doi:10.1016/0006-8993(87)90278-2 (1987).

6 Weatherford, S. C., Chiruzzo, F. Y. & Laughton, W. B. Satiety induced by endogenous and exogenous cholecystokinin is mediated by CCK-A receptors in mice. Am J Physiol 262, R574-578, doi:10.1152/ajpregu.1992.262.4.R574 (1992).

7 Miller, L. J., Holicky, E. L., Ulrich, C. D. & Wieben, E. D. Abnormal processing of the human cholecystokinin receptor gene in association with gallstones and obesity. Gastroenterology 109, 1375-1380, doi:10.1016/0016-5085(95)90601-0 (1995).

8 Hewson, G., Leighton, G. E., Hill, R. G. & Hughes, J. The cholecystokinin receptor antagonist L364,718 increases food intake in the rat by attenuation of the action of endogenous cholecystokinin. Br J Pharmacol 93, 79-84, doi:10.1111/j.1476-5381.1988.tb11407.x (1988).

9 Jordan, J. et al. Stimulation of cholecystokinin-A receptors with GI181771X does not cause weight loss in overweight or obese patients. Clin Pharmacol Ther 83, 281-287, doi:10.1038/sj.clpt.6100272 (2008).

10 Elliott, R. L. et al. Discovery of N-benzyl-2-[(4S)-4-(1H-indol-3-ylmethyl)-5-oxo-1-phenyl-4,5-dihydro-6H-[1,2,4]tri azolo[4,3-a][1,5]benzodiazepin-6-yl]-N-isopropylacetamide, an orally active, gut-selective CCK1 receptor agonist for the potential treatment of obesity. Bioorg Med Chem Lett 20, 6797-6801, doi:10.1016/j.bmcl.2010.08.115 (2010).

11 Gigoux, V. et al. Arginine 197 of the cholecystokinin-A receptor binding site interacts with the sulfate of the peptide agonist cholecystokinin. Protein Sci 8, 2347-2354, doi:10.1110/ps.8.11.2347 (1999).

12 Escrieut, C. et al. The biologically crucial C terminus of cholecystokinin and the non-peptide agonist SR-146,131 share a common binding site in the human CCK1 receptor. Evidence for a crucial role of Met-121 in the activation process. J Biol Chem 277, 7546-7555, doi:10.1074/jbc.M108563200 (2002).

13 Archer-Lahlou, E. et al. Molecular mechanism underlying partial and full agonism mediated by the human cholecystokinin-1 receptor. J Biol Chem 280, 10664-10674, doi:10.1074/jbc.M409451200 (2005).

14 Archer-Lahlou, E. et al. Modeled structure of a G-protein-coupled receptor: The

Cholecystokinin-1 receptor. J Med Chem 48, 180-191, doi:10.1021/jm049886y (2005).

15 Miller, L. J. & Gao, F. Structural basis of cholecystokinin receptor binding and regulation. Pharmacol Ther 119, 83-95, doi:10.1016/j.pharmthera.2008.05.001 (2008).

16 Rasmussen, S. G. et al. Crystal structure of the beta2 adrenergic receptor-Gs protein complex. Nature 477, 549-555, doi:10.1038/nature10361 (2011).

17 Zhang, Y. et al. Cryo-EM structure of the activated GLP-1 receptor in complex with a G protein. Nature 546, 248-253, doi:10.1038/nature22394 (2017).

18 Kang, Y. et al. Cryo-EM structure of human rhodopsin bound to an inhibitory G protein. Nature 558, 553-558, doi:10.1038/s41586-018-0215-y (2018).

19 Kato, H. E. et al. Conformational transitions of a neurotensin receptor 1-Gi1 complex. Nature 572, 80-85, doi:10.1038/s41586-019-1337-6 (2019).

20 Yang, F. et al. Structural basis of GPBAR activation and bile acid recognition. Nature, doi:10.1038/s41586-020-2569-1 (2020).

21 Maeda, S., Qu, Q., Robertson, M. J., Skiniotis, G. & Kobilka, B. K. Structures of the M1 and M2 muscarinic acetylcholine receptor/G-protein complexes. Science 364, 552-557, doi:10.1126/science.aaw5188 (2019).

22 Kim, K. et al. Structure of a Hallucinogen-Activated Gq-Coupled 5-HT2A Serotonin Receptor. Cell 182, 1574-1588 e1519, doi:10.1016/j.cell.2020.08.024 (2020).

23 Qiao, A. et al. Structural basis of Gs and Gi recognition by the human glucagon receptor. Science 367, 1346-1352, doi:10.1126/science.aaz5346 (2020).

24 Okashah, N. et al. Variable G protein determinants of GPCR coupling selectivity. Proc Natl Acad Sci U S A 116, 12054-12059, doi:10.1073/pnas.1905993116 (2019).

25 Rose, A. S. et al. Position of transmembrane helix 6 determines receptor G protein coupling specificity. J Am Chem Soc 136, 11244-11247, doi:10.1021/ja5055109 (2014).

26 Hauser, A. S. et al. Pharmacogenomics of GPCR Drug Targets. Cell 172, 41-54 e19, doi:10.1016/j.cell.2017.11.033 (2018).

27 Paulssen, R. H., Fraeyman, N. & Florholmen, J. Activation of phospholipase C by cholecystokinin receptor subtypes with different G-protein-coupling specificities in hormone-secreting pancreatic cell lines. Biochem Pharmacol 60, 865-875, doi:10.1016/s0006-2952(00)00383-x (2000).

28 Wu, V. et al. First intracellular loop of the human cholecystokinin-A receptor is essential for cyclic AMP signaling in transfected HEK-293 cells. J Biol Chem 272, 9037-9042, doi:10.1074/jbc.272.14.9037 (1997).

29 Scemama, J. L. et al. CCK and gastrin inhibit adenylate cyclase activity through a pertussis toxin-sensitive mechanism in the tumoral rat pancreatic acinar cell line AR 4-2J. FEBS Lett 242, 61-64, doi:10.1016/0014-5793(88)80985-2 (1988).

30 Sabbatini, M. E., Bi, Y., Ji, B., Ernst, S. A. & Williams, J. A. CCK activates RhoA and Rac1 differentially through Galpha13 and Galphaq in mouse pancreatic acini. Am J Physiol Cell

Physiol 298, C592-601, doi:10.1152/ajpcell.00448.2009 (2010).

31 Le Page, S. L., Bi, Y. & Williams, J. A. CCK-A receptor activates RhoA through G alpha 12/13 in NIH3T3 cells. Am J Physiol Cell Physiol 285, C1197-1206, doi:10.1152/ajpcell.00083.2003 (2003).

32 Maeda, S. et al. Development of an antibody fragment that stabilizes GPCR/G-protein complexes. Nat Commun 9, doi:ARTN 371210.1038/s41467-018-06002-w (2018).

33 Carpenter, B., Nehme, R., Warne, T., Leslie, A. G. & Tate, C. G. Structure of the adenosine A(2A) receptor bound to an engineered G protein. Nature 536, 104-107, doi:10.1038/nature18966 (2016).

34 Liu, P. et al. The structural basis of the dominant negative phenotype of the Galphai1beta1gamma2 G203A/A326S heterotrimer. Acta Pharmacol Sin 37, 1259-1272, doi:10.1038/aps.2016.69 (2016).

35 Ballesteros, J. A. & Weinstein, H. Integrated methods for the construction of three-dimensional models and computational probing of structure-function relations in G protein-coupled receptors. Meth Neurosci 25, 366-428, doi:10.1016/S1043-9471(05)80049-7 (1995).

36 Shiimura, Y. et al. Structure of an antagonist-bound ghrelin receptor reveals possible ghrelin recognition mode. Nat Commun 11, 4160, doi:10.1038/s41467-020-17554-1 (2020).

37 Wingler, L. M. et al. Angiotensin and biased analogs induce structurally distinct active conformations within a GPCR. Science 367, 888-+, doi:10.1126/science.aay9813 (2020).

38 Hong, C. et al. Structures of active-state orexin receptor 2 rationalize peptide and small-molecule agonist recognition and receptor activation. Nat Commun 12, 815, doi:10.1038/s41467-021-21087-6 (2021).

39 Zhou, F. et al. Molecular basis of ligand recognition and activation of human V2 vasopressin receptor. Cell Res, doi:10.1038/s41422-021-00480-2 (2021).

40 Gigoux, V. et al. Arginine 336 and asparagine 333 of the human cholecystokinin-A receptor binding site interact with the penultimate aspartic acid and the C-terminal amide of cholecystokinin. J Biol Chem 274, 20457-20464, doi:10.1074/jbc.274.29.20457 (1999).

41 Henke, B. R. et al. Optimization of 3-(1H-indazol-3-ylmethyl)-1,5-benzodiazepines as potent, orally active CCK-A agonists. J Med Chem 40, 2706-2725, doi:10.1021/jm970265x (1997).

42 Aquino, C. J. et al. Discovery of 1,5-benzodiazepines with peripheral cholecystokinin (CCK-A) receptor agonist activity. 1. Optimization of the agonist "trigger". J Med Chem 39, 562-569, doi:10.1021/jm950626d (1996).

43 Flock, T. et al. Universal allosteric mechanism for G alpha activation by GPCRs. Nature 524, 173-+, doi:10.1038/nature14663 (2015).

44 DeVree, B. T. et al. Allosteric coupling from G protein to the agonist-binding pocket in GPCRs. Nature 535, 182-186, doi:10.1038/nature18324 (2016).

45 Garcia-Nafria, J. & Tate, C. G. Cryo-EM structures of GPCRs coupled to Gs, Gi and Go. Mol Cell Endocrinol 488, 1-13, doi:10.1016/j.mce.2019.02.006 (2019).

46 Garcia-Nafria, J., Nehme, R., Edwards, P. C. & Tate, C. G. Cryo-EM structure of the serotonin 5-HT1B receptor coupled to heterotrimeric Go. Nature 558, 620-623, doi:10.1038/s41586-018-0241-9 (2018).
47 Kim, H. R. et al. Structural mechanism underlying primary and secondary coupling between GPCRs and the Gi/o family. Nat Commun 11, 3160, doi:10.1038/s41467-020-16975-2 (2020).
48 Albert, P. R. & Robillard, L. G protein specificity: traffic direction required. Cell Signal 14, 407-418, doi:10.1016/s0898-6568(01)00259-5 (2002).
49 Woehler, A. & Ponimaskin, E. G. G protein--mediated signaling: same receptor, multiple effectors. Curr Mol Pharmacol 2, 237-248, doi:10.2174/1874467210902030237 (2009).
50 Koehl, A. et al. Structure of the micro-opioid receptor-Gi protein complex. Nature 558, 547-552, doi:10.1038/s41586-018-0219-7 (2018).
51 Draper-Joyce, C. J. et al. Structure of the adenosine-bound human adenosine A1 receptor-Gi complex. Nature 558, 559-563, doi:10.1038/s41586-018-0236-6 (2018).
52 Duan, J. et al. Cryo-EM structure of an activated VIP1 receptor-G protein complex revealed by a NanoBiT tethering strategy. Nat Commun 11, 4121, doi:10.1038/s41467-020-17933-8 (2020).
53 Zhuang, Y. et al. Structure of formylpeptide receptor 2-Gi complex reveals insights into ligand recognition and signaling. Nat Commun 11, 885, doi:10.1038/s41467-020-14728-9 (2020).
54 Scheres, S. H. RELION: implementation of a Bayesian approach to cryo-EM structure determination. J Struct Biol 180, 519-530, doi:10.1016/j.jsb.2012.09.006 (2012).
55 Kelley, L. A., Mezulis, S., Yates, C. M., Wass, M. N. & Sternberg, M. J. The Phyre2 web portal for protein modeling, prediction and analysis. Nat Protoc 10, 845-858, doi:10.1038/nprot.2015.053 (2015).
56 Pettersen, E. F. et al. UCSF Chimera--a visualization system for exploratory research and analysis. J Comput Chem 25, 1605-1612, doi:10.1002/jcc.20084 (2004).
57 Emsley, P. & Cowtan, K. Coot: model-building tools for molecular graphics. Acta Crystallogr D Biol Crystallogr 60, 2126-2132, doi:10.1107/S0907444904019158 (2004).
58 Croll, T. I. ISOLDE: a physically realistic environment for model building into low-resolution electron-density maps. Acta Crystallogr D Struct Biol 74, 519-530, doi:10.1107/S2059798318002425 (2018).
59 Adams, P. D. et al. PHENIX: a comprehensive Python-based system for macromolecular structure solution. Acta Crystallogr D Biol Crystallogr 66, 213-221, doi:10.1107/S0907444909052925 (2010).
60 Masuho, I., Martemyanov, K. A. & Lambert, N. A. Monitoring G Protein Activation in Cells with BRET. Methods Mol Biol 1335, 107-113, doi:10.1007/978-1-4939-2914-6_8 (2015).
61 Xu, P. et al. Structures of the human dopamine D3 receptor-Gi complexes. Mol Cell 81, 1147-1159 e1144, doi:10.1016/j.molcel.2021.01.003 (2021).
62 Inoue, A. et al. Illuminating G-Protein-Coupling Selectivity of GPCRs. Cell 177, 1933-1947 e1925, doi:10.1016/j.cell.2019.04.044 (2019).

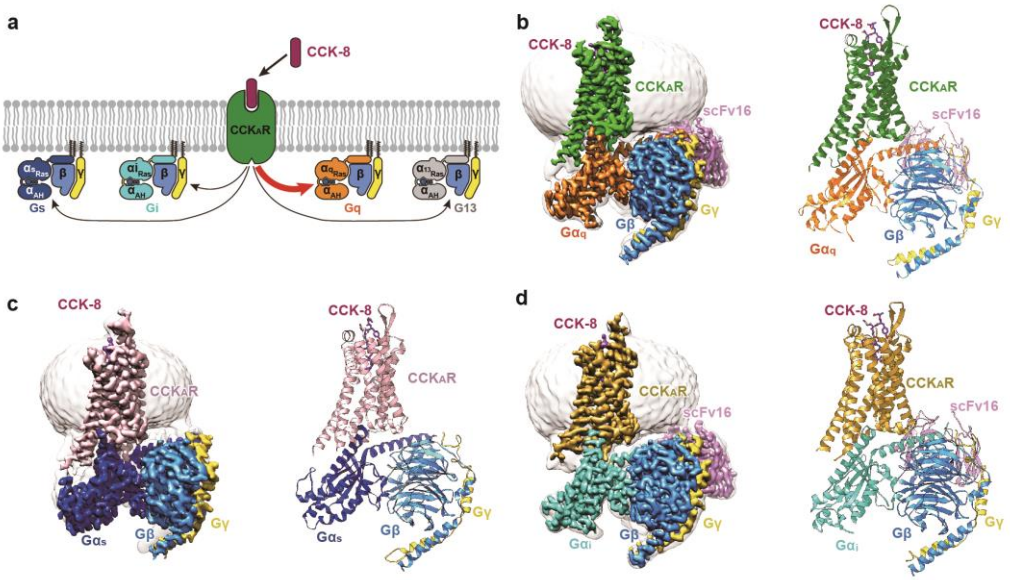

610

Fig. 1 | Cryo-EM structures of CCK_AR–G protein complexes. a, Schematic illustration of G protein coupling promiscuity of CCK_AR. **b-d**, Three-dimensional map (left panel) and the model (right panel) of the CCK-8–CCK_AR–G_q–scFv16 (**b**), CCK-8–CCK_AR–G_s (**c**), and CCK-8–CCK_AR–G_i–scFv16 (**d**) complexes. CCK-8, magenta; CCK_AR (**b**), green; CCK_AR (**c**), pink; CCK_AR (**d**);
615 dark yellow; $G\alpha_q$, orange; $G\alpha_s$, blue; $G\alpha_i$, cyan; Gβ, light blue; Gγ, yellow; scFv16, light purple.

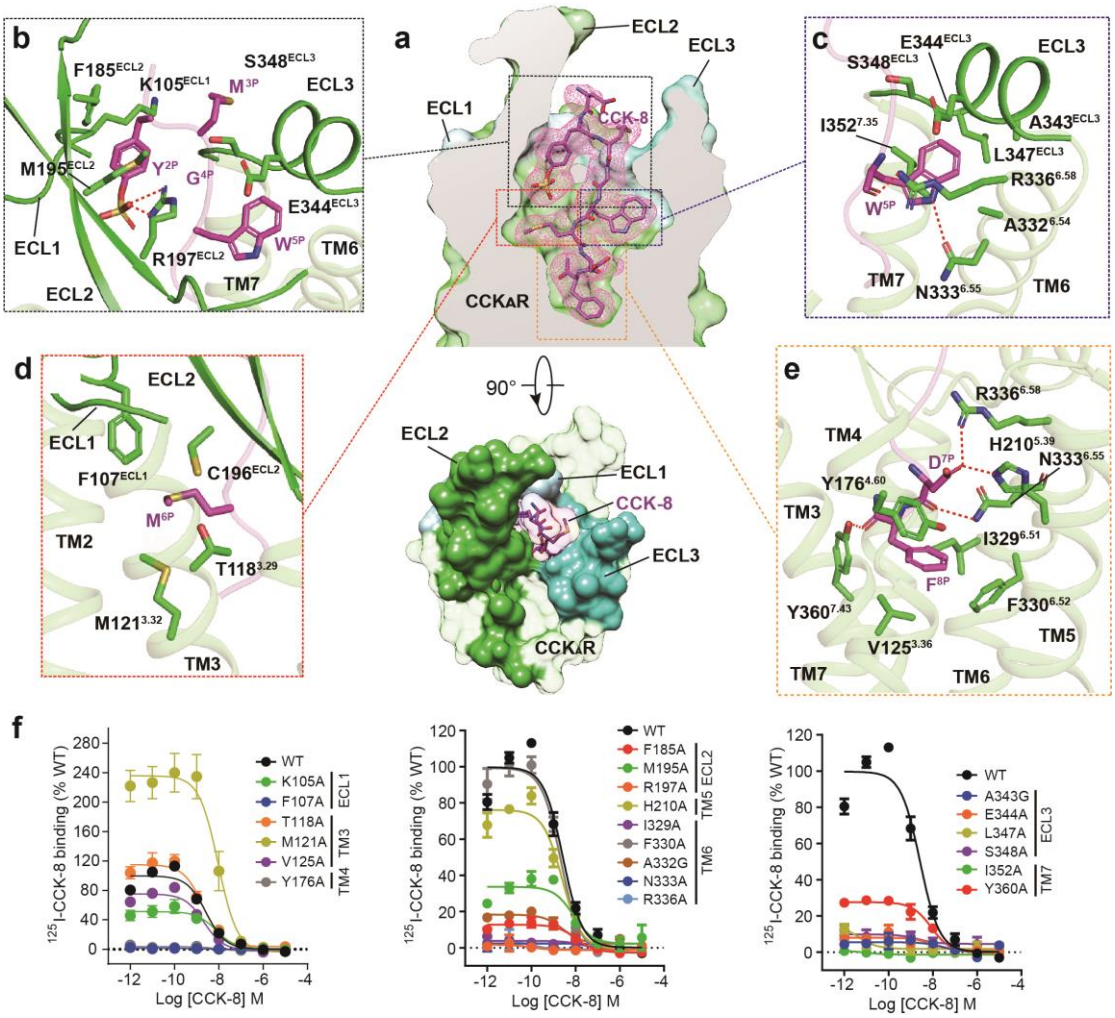

Fig. 2 | Recognition of sulfated CCK-8 by CCK_AR. a, CCK-8 sits in the orthosteric binding pocket of CCK_AR shown at side view (upper panel) and extracellular view (bottom panel). The density map of CCK-8 is shown as magenta mesh, and CCK-8 is displayed as magenta sticks. CCK_AR is shown in green as a cut-away surface (upper panel). ECL1 (light blue), ECL2 (lime green), and ECL3 (turquoise) are highlighted as solid surfaces. **b-e**, Interaction details between sulfated CCK-8 and CCK_AR. **b**, Recognition of CCK-8 by the three extracellular loops. **c**, Recognition of CCK-8 by the deep hydrophobic cavity beneath ECL3. **d**, Recognition of CCK-8 by the shallow hydrophobic cavity beneath ECL1 and ECL2. **e**, Recognition of CCK-8 by the bottom TMD region. Key interaction residues from CCK_AR are shown as green sticks, and the receptor is shown in cartoon presentation. Polar interactions are indicated as red dashed lines. **f**, Effects of mutations in the receptor ligand-binding pocket on CCK-8 binding activity assessed by a radiolabeled ligand binding assay (n=3-4). Competition curves of mutants from ECL1, TM3, TM4 (left), ECL2, TM5, TM6 (middle), ECL3 and TM7 (right) compared to wild-type (WT) CCK_AR are shown.

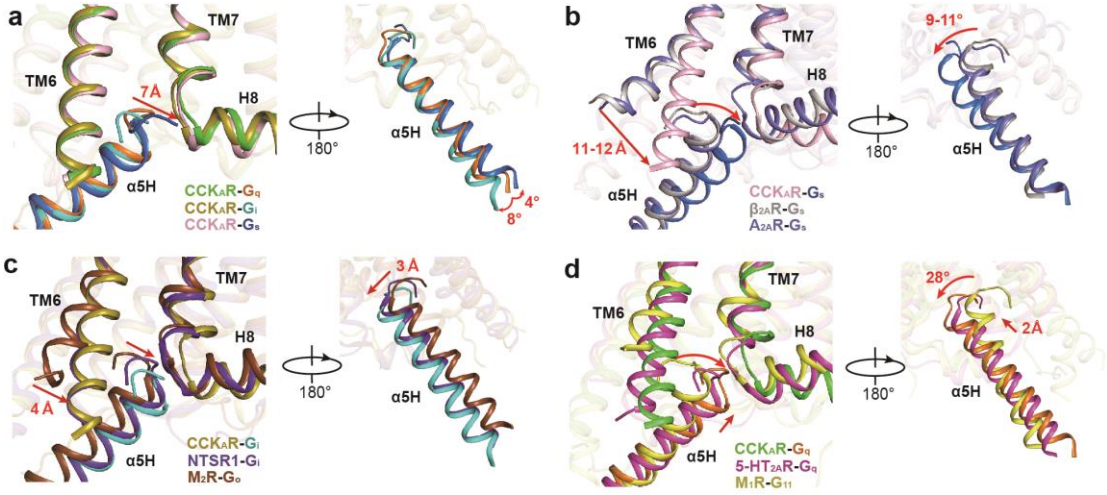

635

Fig. 3 | Structural comparison of TM6 and α5 helix between CCK_AR-G protein complexes and representative G_s-, G_q-, and G_i-coupled GPCR structures in two different views. a, Structural comparison of CCK_AR–G_q, CCK_AR–G_s, and CCK_AR–G_i complexes. A 7 Å movement of the distal end of $G\alpha_s$ α5 helix relative to that of $G\alpha_q$ and swing of Gα α5 helix are highlighted as red
640 arrows. **b**, Structural comparison of CCK_AR–G_s with $\beta_{2A}R$–G_s and $A_{2A}R$–G_s complexes. Red arrows indicate an 11-12 Å displacement of TM6 and a 9-11° swing of Gα α5 helix of G_s-coupled CCK_AR relative to G_s-coupled $\beta_{2A}R$ and $A_{2A}R$. **c**, Structural comparison of CCK_AR–G_i with NTSR1–G_i and M_2R–G_o complexes. A 4 Å inward displacement of TM6 and a 3 Å $G\alpha_i$ α5 helix shift of G_q-coupled CCK_AR in contrast to G_o-coupled M_2R are indicated as red arrows. **d**, Structural comparison of
645 CCK_AR–G_q with 5-$HT_{2A}R$–G_q and M_1R–G_{11} complexes. A 2 Å upward movement of $G\alpha_q$ of G_q-coupled CCK_AR compared to G_q-coupled 5-$HT_{2A}R$ and a 28° rotation relative to G_{11}-coupled M_1R are highlighted as red arrows. The complex structures are aligned based on TM2-TM4 of the receptors. $\beta_{2A}R$–G_s, $A_{2A}R$–G_s, NTSR1–G_i, M_2R–G_o, 5-$HT_{2A}R$–G_q, and M_1R–G_{11} structures (PDB codes: 3SN6, 5G53, 6OS9, 6OIK, 6WHA, and 6OIJ) are colored in gray, marine, purple blue, dark
650 brown, magenta, and yellow, respectively.

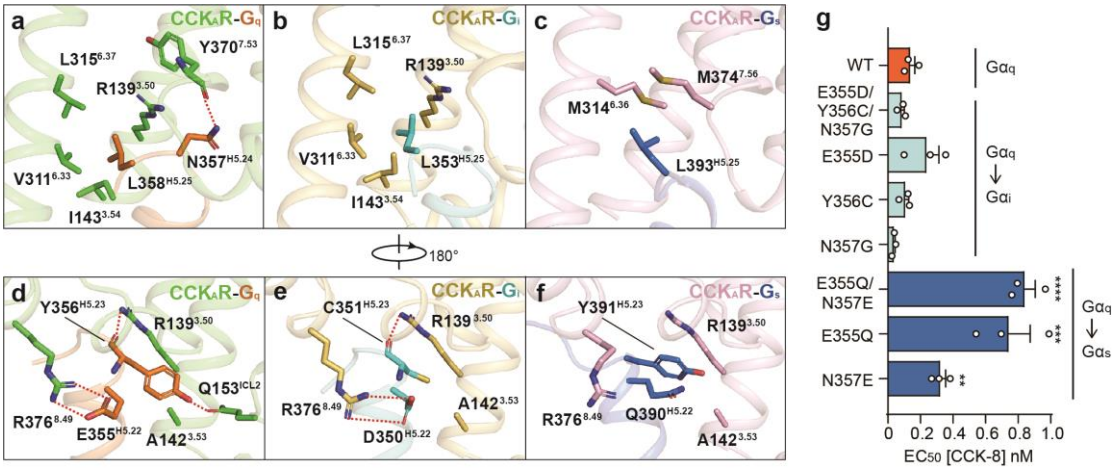

Fig. 4 | Distinct interaction patterns of residues from the "wavy hook" motif. a-c, Interaction details between CCK_AR and $L358^{H5.25}$ and $N357^{H5.24}$ of $G\alpha_q$ (**a**), $L353^{H5.25}$ of $G\alpha_i$ (**b**), and $L393^{H5.25}$ of $G\alpha_s$ subunit (**c**). **d-f**, Interaction details between CCK_AR and $Y356^{H5.23}$ and $E355^{H5.22}$ of $G\alpha_q$ (**d**), $C351^{H5.23}$ and $D350^{H5.22}$ of $G\alpha_i$ (**e**), and $Y391^{H5.23}$ and $Q390^{H5.22}$ of $G\alpha_s$ subunit (**f**). H-bonds and salt bridges are indicated as red dashed lines. **g**, BRET assay evaluating the effects of "wavy hook" substitutions on CCK_AR-G protein coupling. The "wavy hook" residues of the $G\alpha_q$ subunit were displaced by the corresponding residues in $G\alpha_s$ and $G\alpha_i$ subunits. All data were analyzed by one-way ANOVA. $^{****}P<0.0001$, $^{***}P<0.001$, $^{**}P<0.01$.

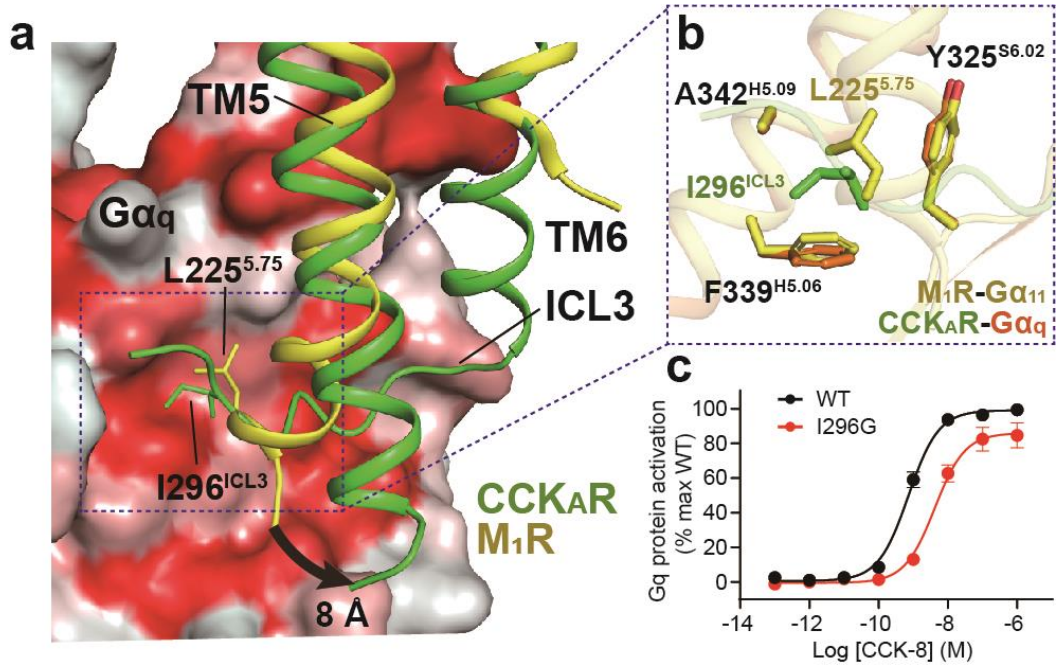

665 **Fig. 5 | Interaction between ICL3 loop of CCK_AR and $G\alpha_q$ subunit. a**, $I296^{ICL3}$ of CCK_AR and $L225^{5.75}$ of M_1R occupy the same hydrophobic sub-pocket of the Gα subunit. The $G\alpha_q$ subunit is shown as a surface presentation by hydrophobicity (hydrophobic surface in red). An 8 Å outward bend of TM5 of CCK_AR relative to that of M_1R is highlighted by a black arrow. **b**, Detailed interactions between $I296^{ICL3}(CCK_AR)/L225^{5.75}(M_1R)$ and hydrophobic patch comprised by 670 $Y325^{S6.02}$, $F339^{H5.06}$, and $A342^{H5.09}$ of $G\alpha_q$ and $G\alpha_{11}$ subunits. **c**, BRET assay indicates that I296G mutation decreases the association rate of CCK_AR with G_q heterotrimer (n=3). WT, wild-type.

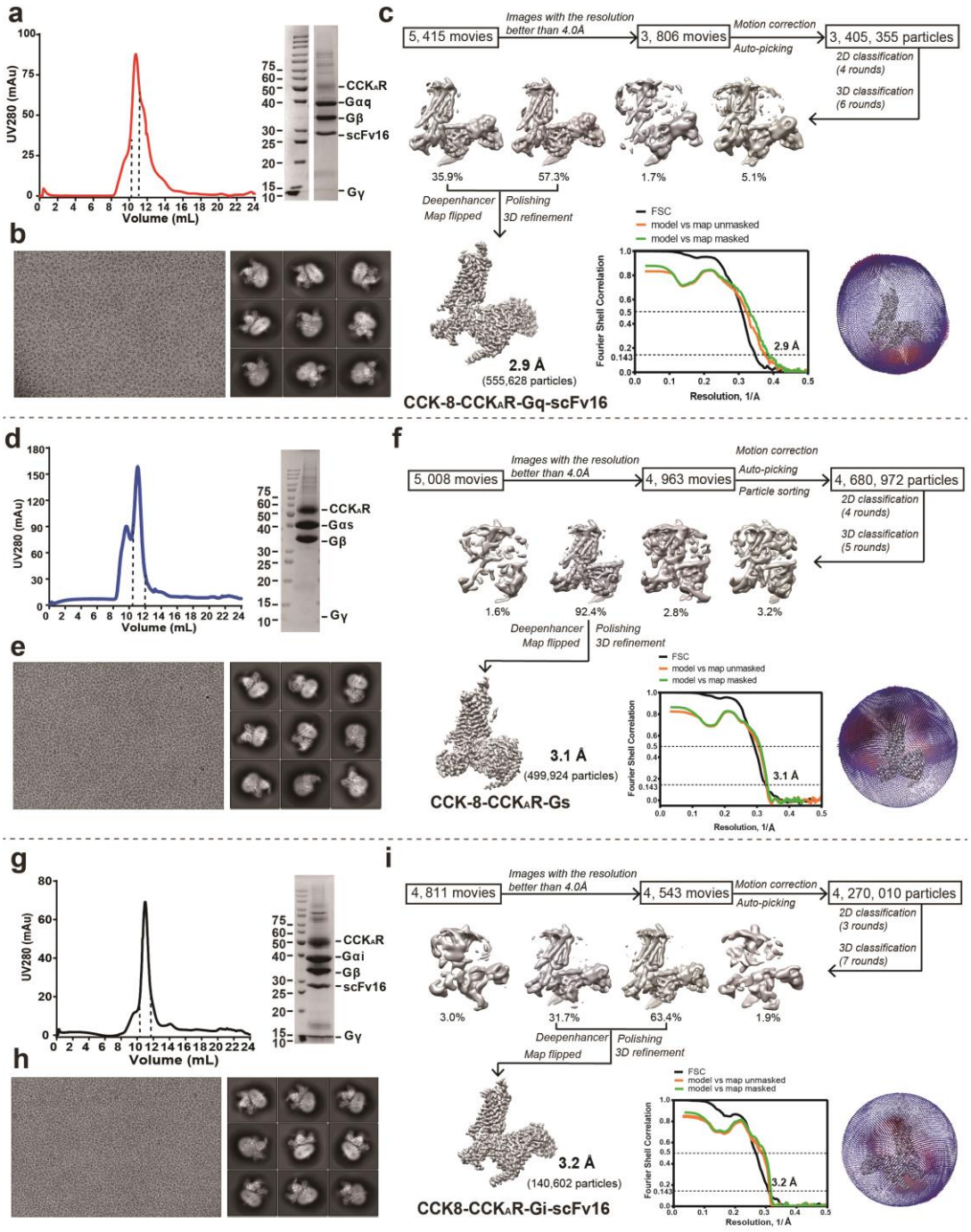

675 **Extended Data Fig. 1 | Cryo-EM workflows for structure determination of CCK_AR–G protein complexes. a**, Size exclusion chromatography (SEC) profile and SDS-PAGE analysis of the CCK-8–CCK_AR–G_q–scFv16 protein complex sample. **b**, Representative cryo-EM micrograph and 2D classification averages of the CCK-8–CCK_AR–G_q–scFv16 complex, the 2D averages display different secondary features in different views. **c**, Single-particle cryo-EM data processing
680 flowcharts of the CCK-8–CCK_AR–G_q–scFv16 by Relion 3.1, including the Euler angle distribution of particles used in the final refinement and the fourier shell correlation (FSC) curves. The global resolution defined at the FSC=0.143 is 2.9 Å. **d**, Size exclusion chromatography (SEC) profile and

SDS-PAGE analysis of the CCK-8–CCK_AR–G_s protein complex sample. **e**, Representative cryo-EM micrograph and 2D classification averages of the CCK-8–CCK_AR–G_s complex. **f**, Single-particle cryo-EM data processing flowcharts of the CCK-8–CCK_AR–G_s by Relion 3.0, including the Euler angle distribution of particles used in the final refinement and the fourier shell correlation (FSC) curves. The global resolution defined at the FSC=0.143 is 3.1 Å. **g**, Size exclusion chromatography **(**SEC) profile and SDS-PAGE analysis of the CCK-8–CCK_AR–G_i–scFv16 protein complex sample. **h**, Representative cryo-EM micrograph and 2D classification averages of the CCK-8–CCK_AR–G_i–scFv16 complex. **i**, Single particle cryo-EM data processing flowcharts of the CCK-8–CCK_AR–G_i–scFv16 by Relion 3.0, including the Euler angle distribution of particles used in the final refinement and the fourier shell correlation (FSC) curves. The global resolution defined at the FSC=0.143 is 3.2 Å.

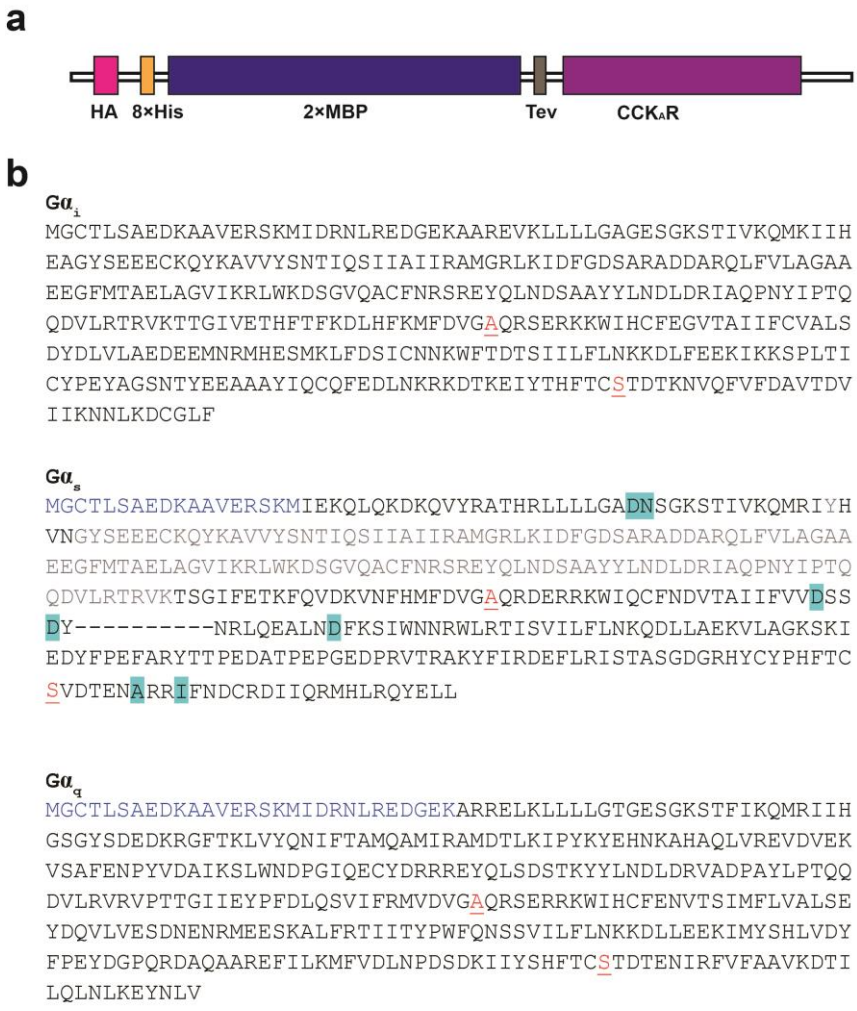

695

Extended Data Fig. 2 | Receptor and Gα subunits used in the cryo-EM structure determination. a, A schematic illustration of the CCK_AR construct used in cryo-EM studies. HA, hemagglutinin signal sequence; 2×MBP, double-MBP tag. **b**, Protein sequences of $G\alpha_q$, $G\alpha_s$, and $G\alpha_{i1}$ subunits. N-terminal sequence replaced in $G\alpha_s$ and $G\alpha_q$ is shown in blue. The two dominant-negative mutations are colored red and underlined. Stabilization mutations derived from the reported mini-$G\alpha_s$ are highlighted in cyan. AHD domain of the $G\alpha_s$ is replaced with the equivalent region of $G\alpha_{i1}$ and colored in gray.

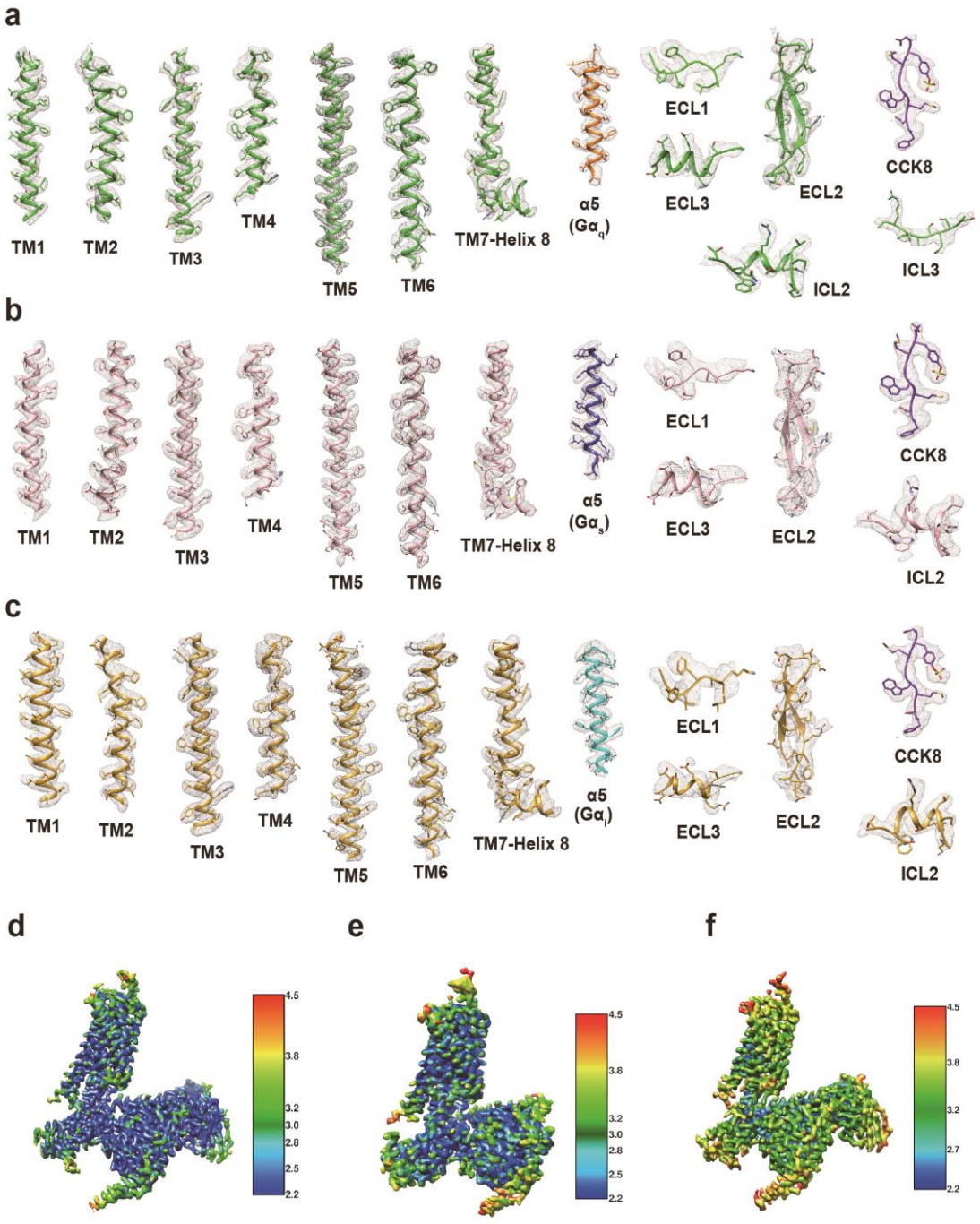

Extended Data Fig. 3 | Local cryo-EM density maps of CCK_AR–G protein complexes. a, Cryo-EM density maps of TM1-TM7, ECL1-ECL3, ICL2, ICL3, CCK-8 peptide and α5 helix of $G\alpha_q$ in the CCK-8–CCK_AR–G_q–scFv16 structure. **b**, Cryo-EM density maps of TM1-TM7, ECL1-ECL3, ICL2, CCK-8 peptide and α5 helix of $G\alpha_s$ in the CCK-8–CCK_AR–G_s structure. **c**, Cryo-EM density maps of TM1-TM7, ECL1-ECL3, ICL2, CCK-8 peptide and α5 helix of $G\alpha_i$ in the CCK-8–CCK_AR–G_i–scFv16 structure. **d-f**, The global density maps of the CCK-8–CCK_AR–G_q–scFv16 (**d**), CCK-8–CCK_AR–G_s (**e**), and CCK-8–CCK_AR–G_i–scFv16 (**f**) colored by local resolution (Å). The density maps are shown at thresholds of 0.08, 0.055 and 0.05 for the CCK_AR–G_q, CCK_AR–G_s and CCK_AR–G_i complex, respectively.

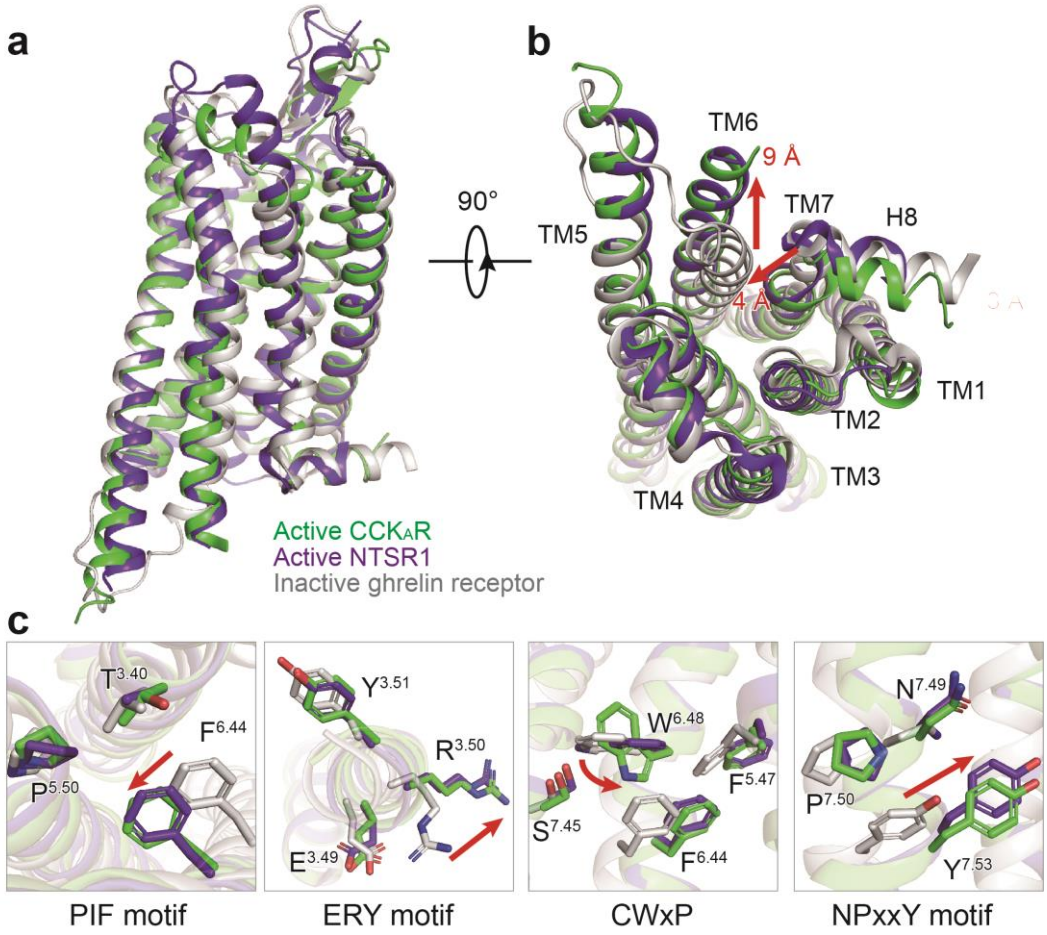

Extended Data Fig. 4 | Active conformation of CCK_AR. a-b, Structural comparison of inactive ghrelin receptor (grey), active NTSR1 (purple blue), and active CCK_AR (green). Side view (**a**) and intracellular view (**b**) of the overall comparison are shown. **c,** Structural rearrangements of key activation motifs (PIF, ERY, CWxP, and NPxxY) in CCK_AR compared to inactive GHSR and active NTSR1. NTSR1, neurotensin receptor 1.

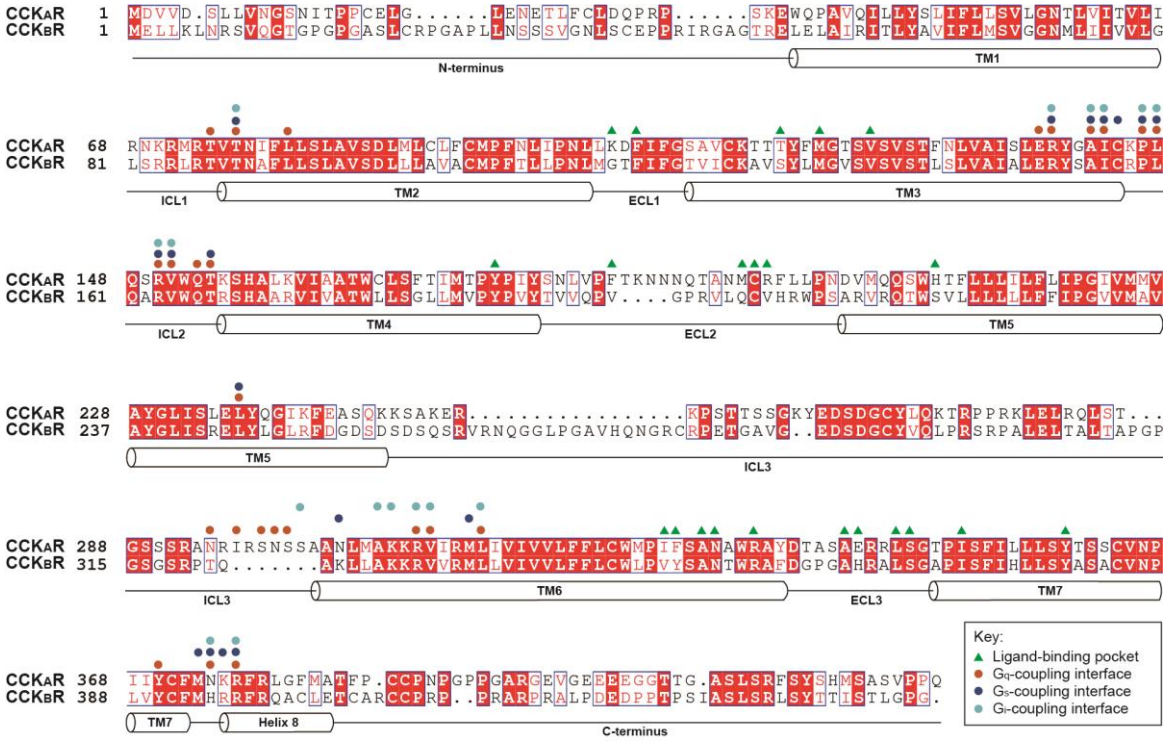

Extended Data Fig. 5 | Sequence alignment of CCK receptors. Helical secondary structures are shown based on CCK_AR. Residues involved in ligand-binding are labeled with green triangles. Residues involved in G protein coupling are labeled with circles (orange, G_q; blue, G_s; cyan, G_i).

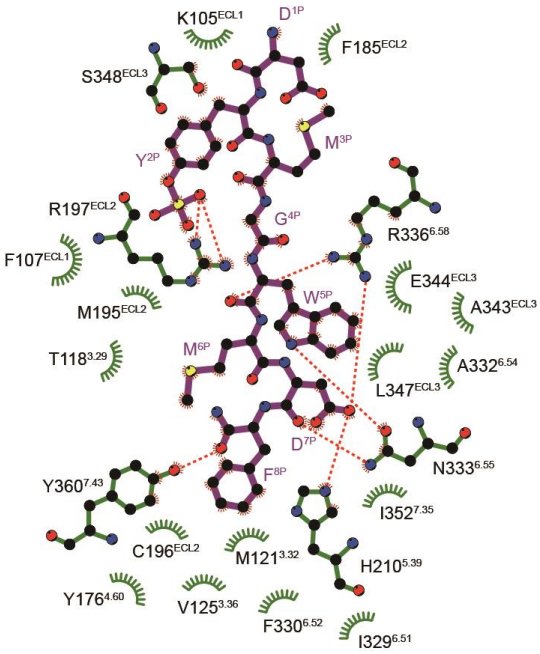

730

Extended Data Fig. 6 | 2D interaction plot of CCK_AR recognition by sulfated CCK-8. Residues in the ligand-binding pocket are colored in green. CCK-8 is displayed as magenta sticks. Polar interactions are indicated as red dashed lines.

735

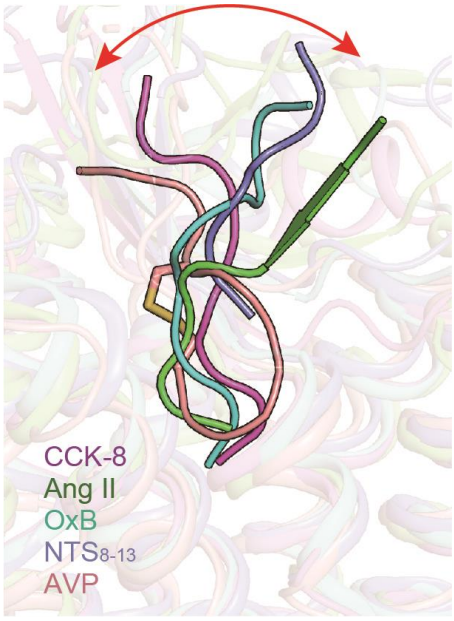

Extended Data Fig. 7 | Structure comparison of CCK-8 with other neuropeptides solved to date. The neuropeptides are shown as a cartoon. The shift of the extracellular part of neuropeptides is highlighted as a red arrow. CCK-8 in the CCK-8–CCK_AR–G_q complex structure, magenta; Ang II, angiotensin II (PDB: 6OS0), green; OxB, orexin B (PDB: 7L1U), cyan; NTS_{8-13}, neurotensin 8-13 (PDB: 6OS9), purple blue; AVP, arginine vasopressin (PDB: 7DW9), salmon.

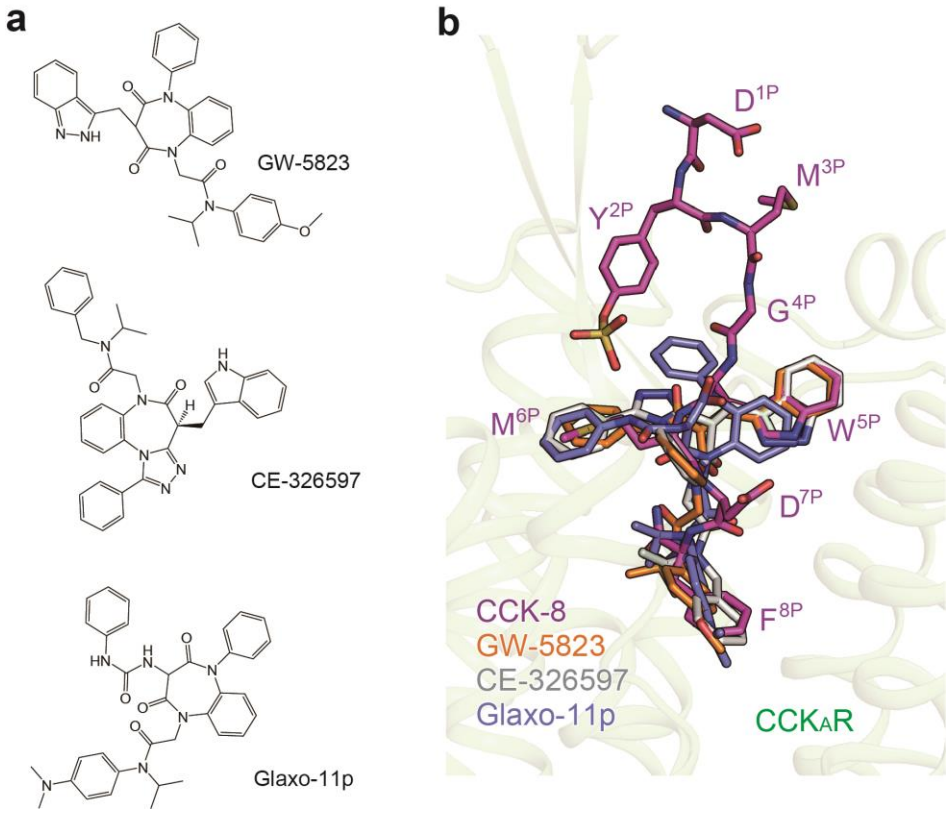

745

Extended Data Fig. 8 | Molecular docking of small molecule agonists to the CCK_AR structure. **a,** Chemical structures of small molecule agonists of CCK_AR. **b,** Comparison of the binding poses of three agonists with CCK-8. CCK-8, magenta; GW-5823, orange; CE-326597, grey; Glaxo-11p, purple blue. CCK-8 and small molecule agonists are shown as sticks. The amino acids of CCK-8 are labelled.

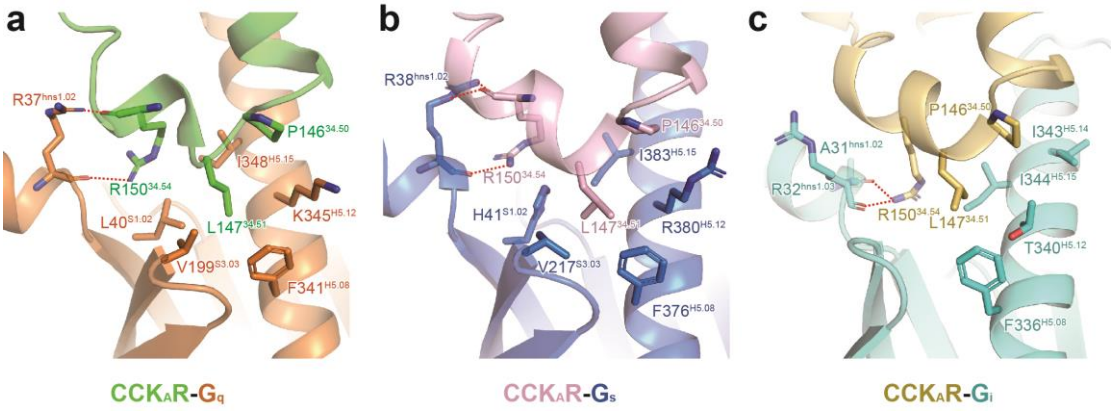

Extended Data Fig. 9 | The interface between CCK$_A$R ICL2 and different G proteins. Detailed interaction between the receptor and Gα_q (**a**), Gα_s (**b**), and Gα_i (**c**) are shown. Side chains of related residues are shown as sticks.

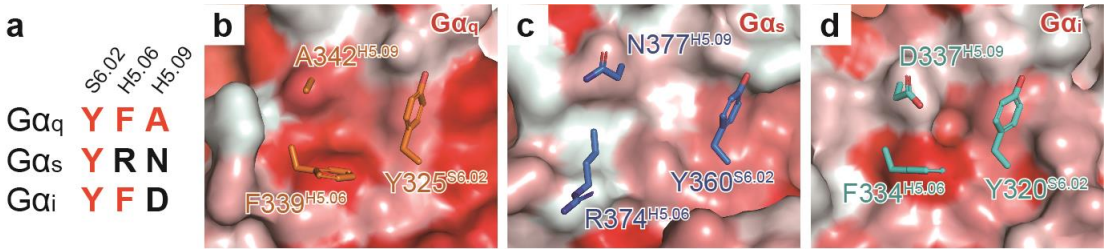

Extended Data Fig. 10 | Comparison of the hydrophobic patch in $G\alpha_q$ subunit to the corresponding sites in other G proteins. a, Sequence alignment of S6.02, H5.06, and H5.09 from $G\alpha_q$, $G\alpha_s$, and $G\alpha_i$ subunits. Residues at positions S6.02, H5.06, and H5.09 comprise the hydrophobic patch to interact with CCK_AR ICL3. **b-d**, Surface presentation of the patch by hydrophobicity. Side chains of residues at positions S6.02, H5.06, and H5.09 in $G\alpha_q$ (**b**), $G\alpha_s$ (**c**), and $G\alpha_i$ (**d**) subunits are shown.

Extended Data Table 1 | Cryo-EM data collection, refinement and validation statistics.

	CCK_AR/G_q/scFv16	CCK_AR/G_s	CCK_AR/G_{i1}/scFv16
Data collection and processing			
Magnification	81,000	81,000	81,000
Voltage (kV)	300	300	300
Electron exposure (e-/ Å2)	80	80	80
Defocus range (μm)	-0.5 ~ -3.0	-0.5 ~ -3.0	-0.5 ~ -3.0
Pixel size (Å)	1.045	1.045	1.045
Symmetry imposed	C1	C1	C1
Initial particle projections (no.)	3, 405, 355	4, 680, 972	4, 270, 010
Final particle projections (no.)	555, 628	499, 924	140, 602
Map resolution (Å)	2.9	3.1	3.2
FSC threshold	0.143	0.143	0.143
Map resolution range (Å)	2.3- 4.3	2.3- 4.3	2.3- 4.3
Refinement			
Initial model used (PDB accession number)	6OIJ	6NBF	6OMM
Model resolution (Å)	3.0	3.2	3.4
FSC threshold	0.5	0.5	0.5
Map sharpening B-factor (Å2)	-97.47	-134.32	-111.38
Model composition			
Non-hydrogen atoms	8999	7196	8860
Protein residues	1170	922	1153
B-factors (Å2)			
Protein	56.03	66.86	63.12
RMSD			
Bond lengths (Å)	0.010	0.010	0.002
Bond angles (°)	1.027	1.010	0.625
Validation			
MolProbity score	1.45	1.39	1.35
Clashscore	4.50	3.85	2.45
Rotamer outliers (%)	0.21	0.26	0.00
Ramachandran Plot			
Favored (%)	96.51	96.57	95.40
Allowed (%)	3.49	3.43	4.60
Disallowed (%)	0.00	0.00	0.00

Extended Data Table 2 | Effects of mutations in the ligand-binding pocket of CCK_AR on CCK-8 binding affinities.

Radiolabeled ligand ([^{125I}]CCK-8) binding assay was performed to evaluate the ligand binding affinity of CCK_AR mutants. Data represent mean pKi ± S.E.M. Experiments were performed in triplicate (n=3-4). *P<0.05 versus wild-type (WT). N.D., not determined. FACS analyses were performed to evaluate the surface expression of the CCK_AR mutants.

Mutant	pKi ± S.E.M.	Expression %
WT	8.58±0.12	100
K105A	7.78±0.22	77.86±6.24
F107A	N.D.	71.85±6.84
T118A	8.73±0.13	78.06±5.38
M121A	8.03±0.15	74.99±5.48
V125A	8.68±0.12	46.48±1.03
Y176A	N.D.	26.63±2.43
F185A	7.98±0.24	77.98±4.85
M195A	8.10±0.26	85.45±4.52
C196A	N.D.	3.24±0.06
R197A	N.D.	104.14±5.14
H210A	8.61±0.12	81.19±4.32
I329A	N.D.	74.22±7.37
F330A	8.67±0.09	27.31±2.74
A332G	8.43±0.12	32.50±4.21
N333A	N.D.	63.96±3.31
R336A	N.D.	82.96±5.35
A343G	N.D.	50.61±5.37
E344A	N.D.	88.00±13.77
L347A	N.D.	52.59±1.43
S348A	N.D.	98.35±8.18
I352A	N.D.	80.35±1.26
Y360A	8.00±0.09	82.85±6.85

Extended Data Table 3 | Coupling activity of CCK_AR with different G proteins.

BRET assay was performed to evaluate the coupling activity of CCK_AR with different G proteins. Data represent mean pEC_{50} ± S.E.M. Decreased fold of E_{max} compared to G_q was calculated. Radiolabeled ligand binding assay was used to evaluate the allosteric effects of different G proteins on the binding affinity of CCK-8. The binding affinities are indicated as pKi ± S.E.M. All data were analyzed by two-tailed Student's *t*-test. **P*<0.05 versus receptor. Experiments were performed in triplicate (n=3).

Group	pEC_{50} ± S.E.M.	Decreased fold of E_{max}	pKi ± S.E.M.
Receptor	—	—	7.92 ± 0.06
Receptor + G_q	8.42 ± 0.08	1	8.28 ± 0.08*
Receptor + G_i	7.32 ± 0.22	6.60	7.87 ± 0.07
Receptor + G_s	7.92 ± 0.65	20.33	8.02 ± 0.06

Extended Data Table 4 | Effect of I296G mutation of CCK_AR on G protein-coupling activity. BRET based NanoBiT G-protein recruitment and NanoBiT G-protein dissociation assays were performed to evaluate G_q-, G_i-, and G_s-coupling activity, respectively. Data represent mean pEC_{50} ± S.E.M. ***P*<0.01 versus wild-type (WT). FACS analyses were performed to evaluate the surface expression of CCK_AR mutant. Radiolabeled ligand binding assay was used to evaluate the effects of the mutation on the binding affinity of CCK-8. The binding affinities are indicated as pKi ± S.E.M. All data were analyzed by two-tailed Student's *t*-test. Experiments were performed in triplicate (n=3).

Mutant	pEC_{50} ± S.E.M.			Expression %	pKi ± S.E.M.
	G_q	G_i	G_s		
WT	9.14 ± 0.04	6.81 ± 0.12	10.48 ± 0.10	100	8.58 ± 0.12
I296G	8.38 ± 0.09**	6.66 ± 0.08	10.46 ± 0.20	99.52 ± 3.10	8.63 ± 0.13